

Utah State University

DigitalCommons@USU

All Graduate Theses and Dissertations

Graduate Studies

5-2023

Low-Erosion Nozzle Materials for Long-Duration Hybrid Rocket Burns

Russell S. Babb
Utah State University

Follow this and additional works at: <https://digitalcommons.usu.edu/etd>



Part of the [Aerospace Engineering Commons](#)

Recommended Citation

Babb, Russell S., "Low-Erosion Nozzle Materials for Long-Duration Hybrid Rocket Burns" (2023). *All Graduate Theses and Dissertations*. 8727.

<https://digitalcommons.usu.edu/etd/8727>

This Thesis is brought to you for free and open access by the Graduate Studies at DigitalCommons@USU. It has been accepted for inclusion in All Graduate Theses and Dissertations by an authorized administrator of DigitalCommons@USU. For more information, please contact digitalcommons@usu.edu.



LOW-EROSION NOZZLE MATERIALS FOR LONG-DURATION HYBRID ROCKET

BURNS

by

Russell S. Babb

A thesis submitted in partial fulfillment
of the requirements for the degree

of

MASTER OF SCIENCE

in

Aerospace Engineering

Approved:

Stephen A. Whitmore, Ph.D.
Major Professor

David K. Geller, Ph.D.
Committee Member

Geordie Richards, Ph.D.
Committee Member

Richard Cutler, Ph.D.
Vice Provost for Graduate Studies

UTAH STATE UNIVERSITY
Logan, Utah

2023

Copyright © Russell S. Babb 2023

All Rights Reserved

ABSTRACT

Low-Erosion Nozzle Materials for Long-Duration Hybrid Rocket Burns

by

Russell S. Babb, Master of Science

Utah State University, 2023

Major Professor: Stephen A. Whitmore, Ph.D.
Department: Mechanical and Aerospace Engineering

Hybrid rocket systems have proven to be a low-cost, safe, practical, and “green” alternative to traditional propellant systems. One major hindrance to hybrid motor performance relates to nozzle throat erosion. The typical operating environment of hybrid systems can lead to nozzle throat erosion due to oxygen-rich exhaust. Additionally, since hybrid systems tend to have a continuous shift in oxidizer-to-fuel ratio the rates of nozzle erosion are highly dependent on motor configuration, flow rates, and burn times. High throat erosion affects motor performance, reliability, and repeatability. To address this shortcoming low-erosion nozzle materials and configurations were evaluated. Pyrolytic graphite was evaluated as throat material for its high-temperature tolerance and thermal conductivity; boron nitride and reinforced carbon-carbon were evaluated as structural and thermal support around the pyrolytic graphite to be used as a heat sink and to allow the pyrolytic graphite to remain cooler for longer, delaying the onset of pyrolyzation and throat erosion. Multiple generations of nozzle designs were tested, and the results of long-duration burns show a five-fold decrease in erosion rates under similar burn conditions when compared to isomolded graphite nozzles.

(63 pages)

PUBLIC ABSTRACT

Low-Erosion Nozzle Materials for Long-Duration Hybrid Rocket Burns

Russell S. Babb

Hybrid rocket systems, which employ a solid fuel grain and a liquid oxidizer, are a low-cost and environmentally friendly alternative to traditional rocket systems. However, hybrid rockets suffer from an increased nozzle throat erosion rate, which impacts motor performance and reliability. To address this issue several materials and low-erosion nozzle configurations were tested. The results of the testing campaign produced a nozzle that reduce the throat erosion rate five-fold.

ACKNOWLEDGMENTS

I am very thankful for the advice and support of my adviser, Dr. Stephen Whitmore, and my committee, Dr. David Geller and Dr. Geordie Richards. A huge thanks go to the students of the USU Propulsion Lab, who helped with all the testing. Additional thanks go to the teachers, professors, and organizations who helped me along the way, Dr. Charles Swenson and the Center for Space Engineering, Spencer Wendel, Jackson Graham, Kim Olson and the Utah NASA Space Grant Consortium, Dr. David Rosenberg and the Bear River Fellows Program, Dixon Nielson, IEEE Club, Rover Team, Rocket Club, my study group The Rocket Boys, and my family who have always supported me to achieve my dreams. Thanks to my wife for her patience and support.

Russell S. Babb

CONTENTS

	Page
ABSTRACT	iii
PUBLIC ABSTRACT	iv
ACKNOWLEDGMENTS	v
LIST OF TABLES	viii
LIST OF FIGURES	ix
NOTATIONS	xi
ACRONYMS	xiii
1 INTRODUCTION	1
1.1 Effect of Nozzle Erosion Upon Motor Performance	2
1.2 Hybrid Rocket Nozzle Erosion Issues	3
1.3 Reducing Nozzle Throat Erosion	3
1.4 Low-Erosion Composite Nozzle Test Bed Design	5
1.5 Thesis Statement	6
2 LOW-EROSION NOZZLE	7
2.1 Properties of Pyrolytic Graphite [1]	7
2.2 Properties of Hexagonal Boron Nitride [1]	10
2.3 Properties of Reinforced Carbon-Carbon Composite [2]	12
2.4 Thermal Conduction Properties	12
3 EXPERIMENTAL APPARATUS, INSTRUMENTATION, AND TESTING APPARATUS	15
3.1 Low-Erosion Nozzle Test Assembly	15
3.2 Thrust Chamber Assembly	16
3.3 Motor Ignition System	17
3.4 Instrumentation and Test Assembly	19
3.5 Blast Lab Test Stand	20
4 ANALYTICAL MODEL	22
4.1 Modeling of Combustion Chemistry [1,2]	22
4.2 Massflow, O/F, and Equivalence Ratio Calculations [1,2]	24
4.3 Calculating Nozzle Erosion Rate [1,2]	26

5	TESTING SUMMARY	31
5.1	Hot Fire Testing Results	31
5.1.1	Baseline Nozzle Results	31
5.1.2	Low-Erosion Nozzles	34
5.2	Erosion Analysis and Discussion [2]	37
6	CONCLUSION	44
6.1	Future Work	45
	REFERENCES	46

LIST OF TABLES

Table		Page
2.1	Thermal and Mechanical Properties	14
4.1	Enthalpy of Formation for ABS	23
5.1	Summary of Long-Duration Hybrid Nozzle Testing Campaign	32

LIST OF FIGURES

Figure	Page
1.1 Rocket Engine Comparison	2
1.2 Traditional Nozzle Cooling Systems	4
1.3 Low-Erosion Nozzle Cross-Section	5
2.1 Dimensioned Drawing	8
2.2 Low-Erosion Nozzle	9
2.3 Orientation of Pyrolytic Graphite Graphene Sheets	9
2.4 Pyrolytic Graphite Nozzle Throat Stack	10
2.5 Orientation of Hexagonal Boron Nitride	11
2.6 Hexagonal Boron Nitride Insulator	11
2.7 Reinforced Carbon-Carbon Insulator	13
3.1 Comparing Alternative Nozzle Configurations	16
3.2 Cutaway View of Thrust Chamber Assembly Showing Low-Erosion Nozzle Interface Details	16
3.3 Thrust Chamber Components	17
3.4 Test Motor Fuel Grain Configuration	18
3.5 Motor Ignition System for Testing Electronics Layout	19
3.6 Test Systems Plumbing and Instrumentation Diagram (PID)	19
3.7 Annotated Test Stand	20
3.8 National Instruments Labview Virtual Instrument Front Panel	21
3.9 Test Stand Setup in Blast Lab	21
4.1 Generic ABS Chemical Structure	22

4.2 Thermodynamic Properties of GOX/ABS Combustion Products Derived by CEA 24

5.1 Isomolded Graphite Nozzle 1 Test 33

5.2 Isomolded Graphite Nozzle 2 Test 33

5.3 Baseline RCC Nozzle with a Cumulative 32 Seconds of Burn Time 34

5.4 Generation 1 Nozzle 35

5.5 PG-SN Throat Inserts 35

5.6 Generation 2 Nozzle 36

5.7 Generation 2 Nozzle Failure 36

5.8 Generation 3 Nozzle 37

5.9 Postburn Comparisons of PG-SN and PG-HT Nozzle Throat Inserts 38

5.10 Effects of Nozzle Erosion on Calculated Thrust Profiles for Monolithic Iso-
molded Graphite Nozzle 39

5.11 Effects of Nozzle Erosion on Calculated Thrust Profiles for Monolithic RCC
Nozzle 39

5.12 Effects of Nozzle Erosion on Calculated Thrust Profiles for Generation 1
Nozzle Configuration 40

5.13 Effects of Nozzle Erosion on Calculated Thrust Profiles for Generation 2
Nozzle Configuration 40

5.14 Effects of Nozzle Erosion on Calculated Thrust Profiles for Generation 3
Nozzle Configuration 41

5.15 Erosion Onset Time for Various Nozzle Materials 42

5.16 Erosion Rate for Various Nozzle Materials 43

NOTATIONS

Variables

A^*	Throat Cross-sectional Area
A_e	Nozzle Exit Area
C	Carbon
c^*	Characteristic Velocity
C_F	Thrust Coefficient
C_p	Specific Heat
D_0^*	Initial Throat Diameter
$D^*(t)_\varepsilon$	Eroded Throat Diameter
E	Elastic Modulus
F	Thrust
g_0	Gravitational Acceleration
H	Hydrogen
ΔH_{0f}	Total Enthalpy Of Formation
$\Delta H_{fmonomer}$	Enthalpy Contribution From Each Monomer
$\Delta H_{fpolymer}$	Enthalpy Contribution From Each Polymer
I_{sp}	Specific Impulse
\dot{m}	Massflow
\dot{m}_{ox}	Massflow Of Oxidizer
\dot{m}_{fuel}	Massflow Of Fuel
ΔM_{fuel}	Change In Fuel Mass
M_w	Molecular Weight
O/F	oxidizer-to-fuel
\bar{O}/\bar{F}	average oxidizer-to-fuel
N	Nitrogen

N_a	Acrylonitrile
N_b	Butadiene
N_s	Styrene
P_0	Chamber Pressure
P_a	Atmospheric Pressure
P_e	Nozzle Exit Pressure
P_{pox}	Residual Oxygen Pressure
P_r	Prandtl Number
ΔQ_p	Enthalpy of Polymerization From Each Monomer
R_g	Plume Exhaust Gas Constant Of Proportionality
\dot{r}_{tburn}	Throat Area Erosion Rate
T_0	Stagnation/Flame Temperature
t_{burn}	Burn Time
T_{max}	Max Temperature
T_{ox}	Temperature of Oxidization
t_{pyrol}	Pyrolysis Onset Time
V_e	Nozzle Exit Velocity
α	Edge Plane
β	Basal Plane
γ	Specific Heat
η^*	Combustion Efficiency
κ	Thermal Conductivity
μ	Dynamic Viscosity
ν	Poisson's Ratio
ξ	Coefficient of Thermal Expansion
ρ	Density
ε_{A^*}	Linear Throat Area Erosion Rate
Φ	Equivalence Ratio

ACRONYMS

1-D	1 Dimensional
2-D	2 Dimensional
3-D	3 Dimensional
ABS	Acrylonitrile Butadiene Styrene
BN	Boron Nitride
BLAST	Battery and Survivability Limits Testing
CBN	Cubic Boron Nitride
C/C	Layered Graphite-Epoxy, carbon/carbon
CEA	Chemical Equilibrium with Applications
COTS	Commercial Off The Shelf
CTE	Coefficient of Thermal Expansion
FDM	Fused Deposition Modeling
FTIR	Fourier Transform Infrared
GOX	Gaseous Oxygen
HBN	Hexagonal Boron Nitride
HTPB	Hydroxyl-Terminated Polybutadiene
HVPS	High-Voltage Power Supply
H ₂ O ₂	Hydrogen Peroxide
PG	Pyrolytic Graphite
PG-CN	Pyrolytic Graphite Continuously Nucleated
PG-HT	Pyrolytic Graphite High Temperature
PG-SN	Pyrolytic Graphite Substrated Nucleated
PID	Plumbing and Instrumentation Diagram
RCC	Reinforced Carbon-Carbon Composite
SS-316	Stainless Steel 316
USU	Utah State University
NI VI	National Instrument Virtual Instrument

CHAPTER 1

INTRODUCTION

Hybrid rocket systems have inherently safe characteristics and are environmentally friendly especially when compared to traditional propellant systems, which employ extremely toxic or hazardous propellants [3]. The complexity of hybrid systems is comparable to that of monopropellant systems as they both require only a single fluid flow path, but typically hybrid motors are able to achieve higher performance [4]. They are able to be a low-cost replacement to the traditional propellant systems. Hybrid rocket systems are being proposed and tested in multiple applications including launch vehicles, sounding rockets [5, 6], orbital insertion for small-to-medium class satellites [7, 8], as upper stages for Nano-launchers [9], and as a surface launch system for Lunar and Mars sample return missions [10].

Hybrid systems occupy the middle ground between solid rocket motors and bipropellant liquid motors. The hybrid has a lower mass fraction (wet mass/dry mass) than solid but is able to do real-time throttling [11, 12], on-demand ignition, shut-down, and re-ignition [13–16]. This allows for precise guidance, trajectory adjustments, and station keeping. Hybrid systems have higher mass fractions compared to bipropellant due to using only a single fluid flow path allowing them to be simpler than bipropellant. Hybrid rocket systems have the potential to significantly out-perform solid propellant systems [17] while having similar performance and less complexity than bipropellant liquid systems. Figure 1.1 shows the difference between liquid, solid and hybrid engines.

However, hybrid rocket systems have several challenges. Several researchers have investigated trajectory optimization with hybrid propulsion systems [9, 18–20]. The primary conclusion showed that model uncertainties result in significant performance deviations from nominal prediction. In some cases there were such large deviations that the mission objectives could not be achieved. Uncertainty in nozzle throat erosion of hybrid motors is

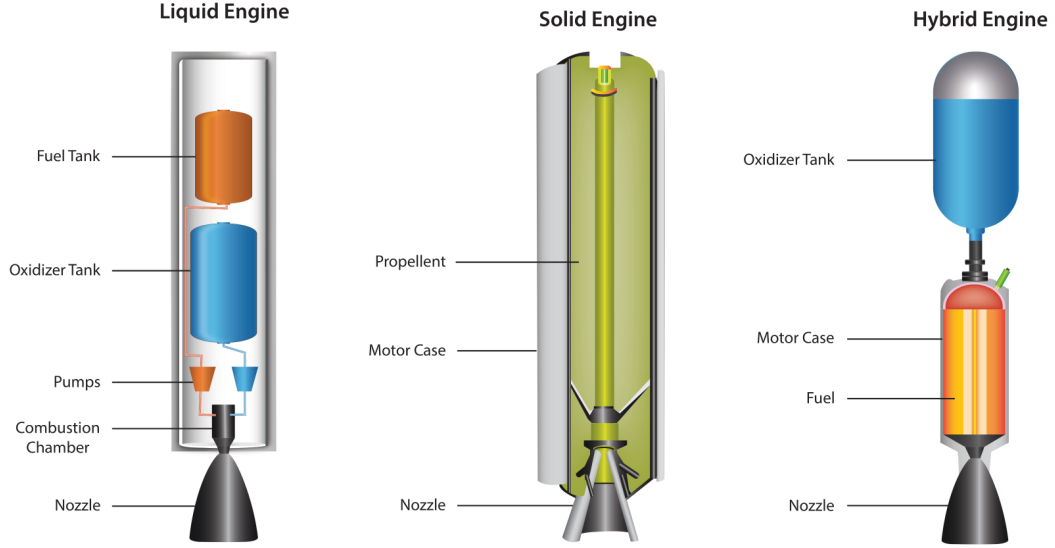


Fig. 1.1: Rocket Engine Comparison

a primary contributor to these uncertainties in performance. Resolving nozzle erosion will improve hybrid motor performance and increase reliability of hybrid motor models.

1.1 Effect of Nozzle Erosion Upon Motor Performance

Motor chamber pressure P_0 is the primary measurement for real-time propulsion system performance feedback and control since in-flight thrust and vehicle mass cannot be measured in real time. Chamber pressure is linked through the thrust coefficient C_F to performance parameters such as thrust F , massflow \dot{m} , and specific impulse I_{sp} through Eqs. (1.1) - (1.3). Typically prelaunch testing or previous flight data is analyzed to derive C_F . Instantaneous throat cross-section area A^* is critical for accurate calculations. Uncertainty in instantaneous throat area directly contributes to the uncertainty in calculating motor thrust and nozzle exit \dot{m} . Characterization and reduction of nozzle throat erosion will improve the characterization and modeling of hybrid motors.

$$C_f = \frac{F}{P_0 A^*} \quad (1.1)$$

$$F = \dot{m}V_e + (P_e - P_a)A_e \quad (1.2)$$

$$I_{sp} = \frac{F}{\dot{m}g_0} \quad (1.3)$$

The effects of nozzle erosion, and the direct influence on throat area uncertainty, compromise the accurate simulation and design of further hybrid systems and have been understudied. Nozzle erosion uncertainty increases with longer burn duration. The continuous throat erosion affects the thrust profile, consumed propellant and oxidizer mass, along with other performance characteristics. To provide accurate hybrid motor system simulation, design, and trajectory optimization, it is essential to address nozzle erosion [21].

1.2 Hybrid Rocket Nozzle Erosion Issues

It was assumed that nozzle throat erosion and ablative cooling for hybrid motors would be similar to solid propellant rocket motors, using similar materials and getting similar results. However, due to the differences in the operating environments of hybrids and solids, this assumption is not valid. Solid rocket motors operate in a slightly fuel-rich environment, eliminating unburned oxygen, which is highly reactive with nozzle throat material. Due to the nature of how hybrid rockets burn with solid fuel and liquid oxidizer, they have a continual oxidizer-to-fuel (O/F) ratio shift throughout their burn profile. Typically, hybrid motors shift to a lean condition [22], allowing high-temperature oxygen-rich exhaust to form and react with nozzle materials. Hybrid motors are ultimately exposed to higher temperatures and greater concentrations of oxygen in the exhaust compared to solid motors, resulting in erosion rates that can be as much as two to three times higher than equivalently sized solids [23, 24].

1.3 Reducing Nozzle Throat Erosion

One approach to reducing nozzle throat erosion for hybrid rockets is to use a material that can survive the environment without reacting with oxygen. Hybrid rocket exhaust can

be up to $3000\text{ }^{\circ}\text{C}$ and contains high concentrations of oxygen. This operating environment is extremely difficult to design for, leaving typical materials such as layered graphite-epoxy (carbon/carbon, C/C)—which can survive temperatures up to $3000\text{ }^{\circ}\text{C}$ but rapidly oxidizes above $650\text{ }^{\circ}\text{C}$ with oxygen present—inappropriate for the application with no viable oxidative resistant coatings available at this temperature range. Low-erosion refractory materials could possibly be used but due to the added mass, it would incur a considerable dry mass penalty.

Another approach is to conduct or convect heat away from the throat thus delaying the onset of pyrolysis. An active method for cooling the nozzle, one that is integrated into many large liquid bipropellant systems, is to use propellant to convect heat away from the nozzle structure by passing the propellant through tubes that surround, or are part of, the nozzle before the propellant is injected into the combustion chamber [25]. A passive method would be to increase the thermal conduction away from the nozzle throat through the nozzle structure to dissipate it through radiation or into a thermal heat sink. Figure 1.2 shows cross-sections for ablative cooling used in solid motors along with film and channel cooling used in liquid motors.

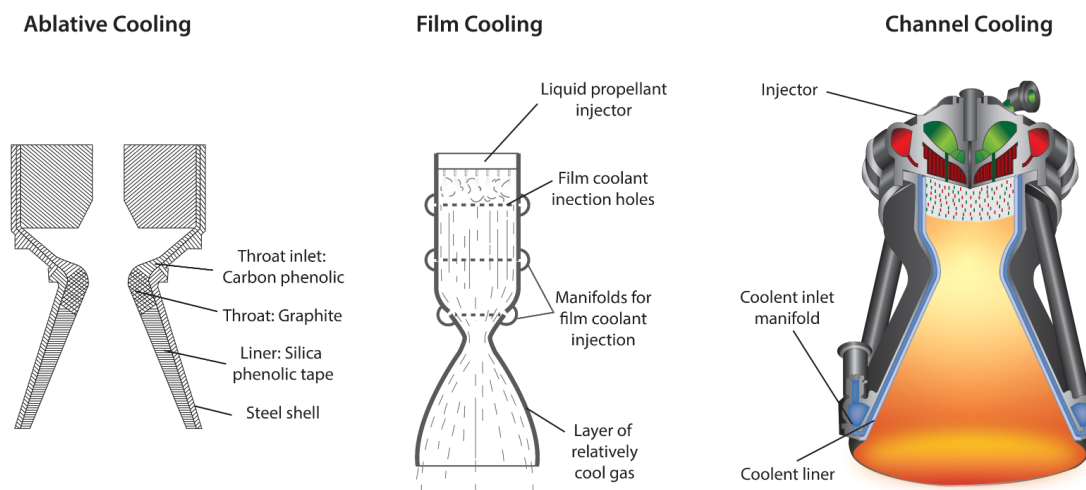


Fig. 1.2: Traditional Nozzle Cooling Systems

1.4 Low-Erosion Composite Nozzle Test Bed Design

The approach pursued in this research is to design a low-erosion composite nozzle for the high-oxidative environment of hybrid motors that takes advantage of multiple materials whose differing properties complement each other in reducing nozzle throat erosion. The throat material would conduct heat away from the inner surface of the throat, keeping that surface at a lower temperature and reducing pyrolysis, and move the heat to a material insulated from the high-oxidative flow that can act as a heat sink. Pyrolytic graphite (PG) was studied for throat material with hexagonal boron nitride (HBN) or reinforced carbon-carbon composite (RCC) as insulating layer materials. Figure 1.3 shows the configuration for the PG throat and the HBN insulating layer. Stainless steel was used for ground testing structural purposes. The HBN was replaced with RCC and the stainless steel shell was not used.

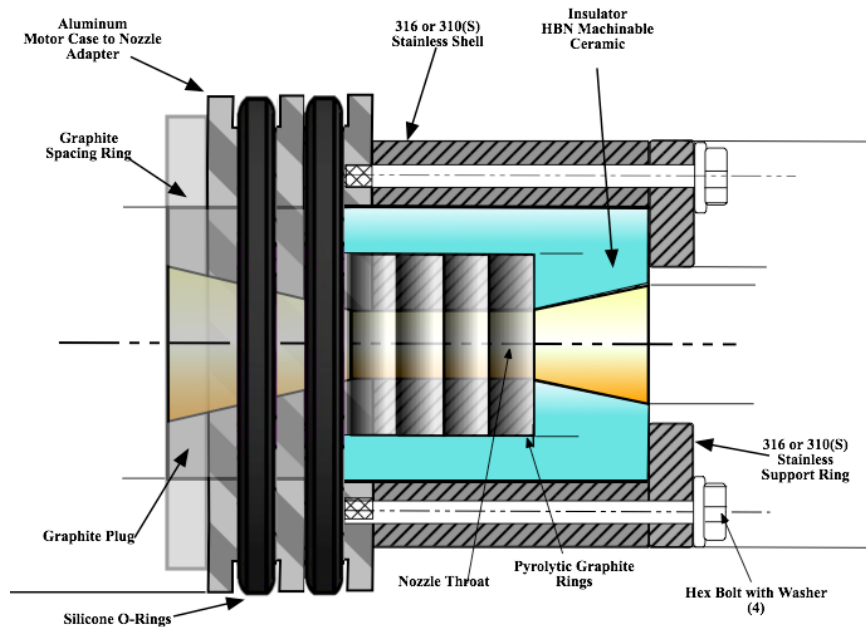


Fig. 1.3: Low-Erosion Nozzle Cross-Section

1.5 Thesis Statement

In order to effectively predict the performance of hybrid rocket systems, it is necessary to develop accurate throat erosion models. Additionally, it is necessary to develop techniques to improve material survivability and reduce erosion rates of the throat. This thesis deals with the in situ material testing of PG, HBN, and RCC for the development of erosion models and a low-erosion nozzle configuration.

CHAPTER 2

LOW-EROSION NOZZLE

This chapter summarizes the material used for three low-erosion nozzle configurations. Each nozzle configuration was tested as a part of this study. The throat of each low-erosion nozzle configuration was manufactured from PG and was encased in a high heat capacity absorbing layer. Two types of PG were used for throat material, PG substrate nucleated (PG-SN) and PG high-conductivity substrate nucleated (PG-HT). HBN and RCC were investigated as high heat capacity absorbing layer materials. Key material properties of PG, HBN, and RCC will be presented in this chapter.

The low-erosion nozzle system tested in this research leverages the anisotropic thermal conduction properties of two materials. Figure 1.3 shows a cutaway view of the nozzle, Fig. 2.1 shows the dimensions, and Fig. 2.2 shows an assembled nozzle. Using the anisotropic material properties of PG, heat can flow rapidly away from the nozzle throat surface. HBN or RCC, with their high heat capacities, conducts the heat from the PG, keeping the flame surface of the PG at a lower temperature.

2.1 Properties of Pyrolytic Graphite [1]

Pyrolytic graphite is a unique form of synthetic graphite manufactured by decomposing hydrocarbon gases, typically propane or methane, to very high temperatures in the absence of oxygen. This process results in an ultra-pure form of carbon that crystallizes into a series of layered graphene sheets. Graphene is an allotrope of carbon formed as a single layer of atoms in a 2-D hexagonal lattice. Graphene sheets are then layered to produce a strong and temperature-resistant material. Because the graphene sheets crystallize in a planar order, pyrolytic graphite is extremely anisotropic. The anisotropy is caused by the tendency of the individual crystallites to align perpendicular to the deposition surface.

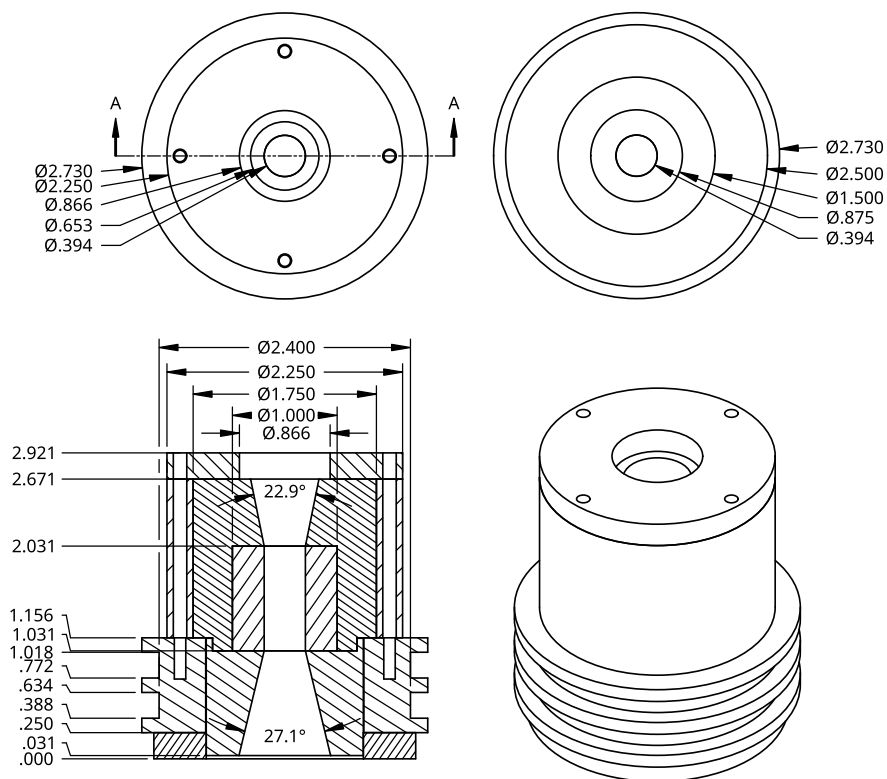


Fig. 2.1: Dimensioned Drawing

Pyrolytic graphite also has high thermal shock resistance and is well suited for the absorption of instantaneous thermal fluxes, as in this application. Most important for this application is the anisotropic property that pyrolytic graphite exhibits a very high thermal conductivity along the direction of the sheet layers, β -radial (basal-plane) direction, and a very low thermal conductivity in the direction perpendicular to the graphene sheets (α -plane). Thus, pyrolytic graphite conducts heat across its α -planar surface like copper and insulates like ceramics in the α -axial (edge-plane) direction. Pyrolytic graphite is one of the best planar conductors of heat currently available. Figure 2.3 shows the orientation of the α - and β -planes in several of the graphene sheets making up pyrolytic graphite, and the relative heat-transfer-rate magnitudes. An example of a nozzle throat stack made from PG is in Fig. 2.4.



Fig. 2.2: Low-Erosion Nozzle

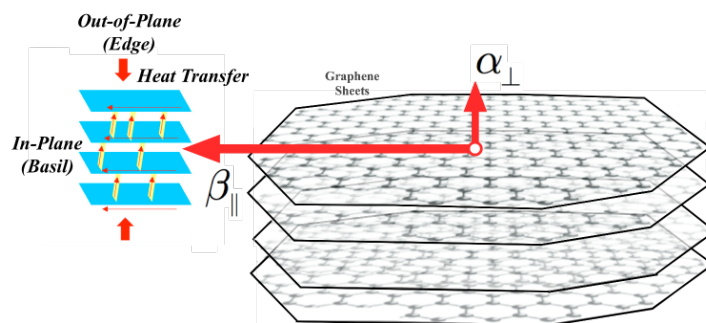


Fig. 2.3: Orientation of Pyrolytic Graphite Graphene Sheets

Generally, PG comes in three different forms; continuously nucleated (CN), substrate nucleated (SN), and high-conductivity substrate nucleated (HT). PG-SN is grown on a substrate uninterrupted whereas PG-CN is continuously interrupted by additional growth nuclei throughout the growth process [26]. The different growth of PG-CN increases thermal



Fig. 2.4: Pyrolytic Graphite Nozzle Throat Stack

conductivity in the β plane and reduces it in the α plane. PG-HT is a thermally annealed version of PG-SN that has increased thermal conductivity by about four times as compared to PG-SN [27].

2.2 Properties of Hexagonal Boron Nitride [1]

Boron nitride (BN) is synthetically produced and exists in various crystalline polymorphs, including cubic and hexagonal. Cubic boron nitride (CBN) is exceptionally hard, harder than diamond, and is commonly used as an abrasive and in cutting tool applications. Hexagonal boron nitride (HBN) is the most stable of the polymorphs. HBN has a layered structure where boron and nitrogen atoms are bound by strong covalent bonds in-plane and each layer is held together by van der Waals forces. Thus HBN, like pyrolytic graphite, exhibits anisotropic properties, with the longitudinal axis (α -plane) value exhibiting a significantly higher value when compared to the radial axis (β -plane). This behavior is the opposite of what is observed for pyrolytic graphite. Unlike CBN, HBN is also sufficiently

soft to be easily machineable. Figure 2.5 shows the orientation of the α - and β -planes, and the relative heat transfer rates in several layers of an HBN structure. An example of a nozzle throat insulator made from HBN is in Fig. 2.6. Important properties associated with HBN are as follows:

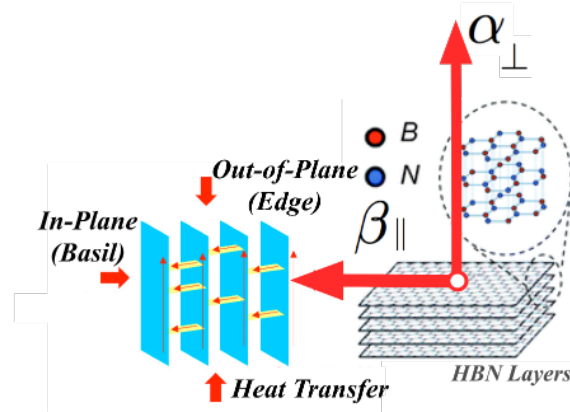


Fig. 2.5: Orientation of Hexagonal Boron Nitride



Fig. 2.6: Hexagonal Boron Nitride Insulator

1. Anisotropic with high thermal conductivity (κ) values along the α -plane and low κ -values along the β -plane.
2. Low thermal expansion coefficient.
3. Good thermal shock and heat resistance.
4. High electrical resistance and low dielectric constant.
5. Easily machined nonabrasive and lubricious.
6. Nontoxic and chemically inert.

2.3 Properties of Reinforced Carbon-Carbon Composite [2]

Reinforced carbon-carbon composite is fabricated by pulling continuous strands of carbon fiber through a die as they are coated in epoxy resin and cured at high speed. Tubes, rods, or bars made by this process align all of the carbon fibers longitudinally along the rod or bar. The resulting material is extremely strong along the longitudinal axis but does not possess the layered structure typical of most RCC composites. Because of the very uniform cross-section, the resulting coefficient of thermal expansion is low and the resulting material also should be significantly more resistant to erosion at high temperatures. RCC also has anisotropic properties that are aligned in the same direction as the PG. An example of a nozzle throat insulator made from RCC is in Fig. 2.7.

2.4 Thermal Conduction Properties

The material properties of the different components tested in this study are in Table 2.1. It must be noted that values of the thermodynamic and material properties as presented in the technical literature show a wide range of variability, especially in regard to the anisotropic materials, PG and HBN. The values presented in Table 2.1 are the result of a selection based on engineering judgment and the quality of reference sources, where values published in technical journals and reference publications are given preference compared to the manufacturer's specification sheets.

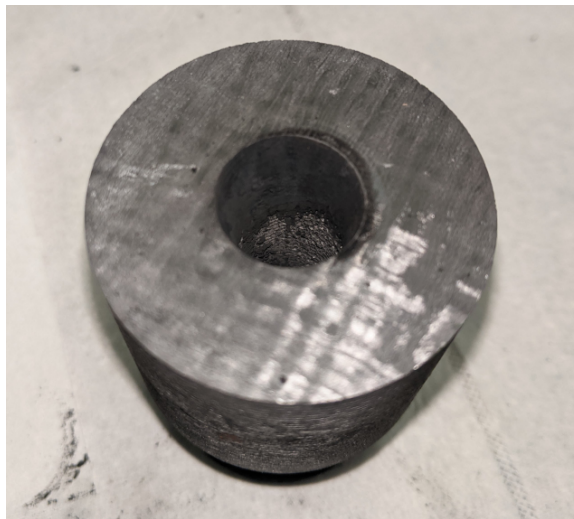


Fig. 2.7: Reinforced Carbon-Carbon Insulator

Table 2.1: Thermal and Mechanical Properties

Material	Operating Temperature	$\kappa, \frac{W}{mK}$ A-B Plane	$\xi, CTE, \frac{mm}{mK}$ A-B Plane	$C_p, \frac{J}{kgK}$	$\rho, \frac{kg}{m^3}$	E, Elastic Modulus GPa A-B plane	Poissons Ratio, ν	Ultimate Tensile Strength, MPa	T_{ox} $^{\circ}C$	T_{max} $^{\circ}C$
HBN-99%	25°C	18.45	0.59	1470	1985	53	0.2	98	850	2500
[28-30]	1650°C	16.8	0.51	3640		13		59		
RCC	25°C	40.3	2.40	712	1450	40	0.14	210	650	3000
[31, 32]	1650°C	32	3.80	2250		80		235		
PG-SN	25°C	400	0.52	710	2190	31	-0.16	152	650	2500
[33-39]	1650°C	114	2.50	2200		24		219		
PG-HT	25°C	1625	1.15	704	2210	80	-0.16	130	845	3000
[34-37, 40]	1650°C	310	4.85	2106		43		187		
SS-316	25°C	13.96	18.60	498.3	7.95	185	0.27	580	925	1700
[41-43]	1000°C	29.24	8.50	628.0		100		370		

CHAPTER 3
EXPERIMENTAL APPARATUS, INSTRUMENTATION, AND TESTING
APPARATUS

A 100 N, 75 mm thruster system previously used by Whitmore et al. [44,45] for hydrogen peroxide (H_2O_2)/acrylonitrile butadiene styrene (ABS) testing was repurposed to use gaseous oxygen (GOX) as the oxidizer. As long as identical equivalence ratios are maintained, hybrid fuel material has little influence on the nozzle erosion rate [24]. Thus, as a time and cost-saving measure, 3-D printed and extruded ABS plastic was used in lieu of hydroxyl-terminated polybutadiene (HTPB) as the fuel for this study.

3.1 Low-Erosion Nozzle Test Assembly

Figure 1.3 shows the schematic of a lab-weight version of the proposed low-erosion nozzle system. Figure 2.1 shows a dimensioned drawing. The layered configuration consists of three major parts: 1) a series of PG-SN [46] disks making up the throat section; 2) a surrounding insulator machined from 99.7% pure HBN [47]; and 3) a shell made from 316-grade stainless steel (SS-316), supporting the entire structure. The layered nozzle system interfaces directly to the existing nozzle motor case adapter, allowing testing without additional modifications. To test a flight-weight version of the HBN nozzle we removed the shell made from stainless steel. An additional configuration was tested by replacing the PG-SN throat with PG-HT along with replacing the HBN insulator with RCC as a drop-in alternative. RCC was an ideal test candidate because of its higher strength and flight heritage. Two configurations were made using RCC. The first is a monolithic RCC nozzle that replaces both the HBN and PG. The second is the PG-HT throat with the RCC being an HBN replacement.

As an experimental control, the three-layer nozzle configuration was replaced with three alternate configurations: 1) a machined graphite plug that matches the PG-SN and

HBN insert dimensions of Fig. 2.1; 2) a whole-nozzle configuration machined entirely from graphite; and 3) a whole nozzle configuration machined entirely from RCC. The graphite plug was inserted into the nozzle adapter of Fig. 1.3. The whole-nozzle graphite configuration featured machined O-ring grooves, allowing the nozzle to be directly mounted into the 75 mm motor case. Figure 3.1 compares some of the different nozzle configurations tested.

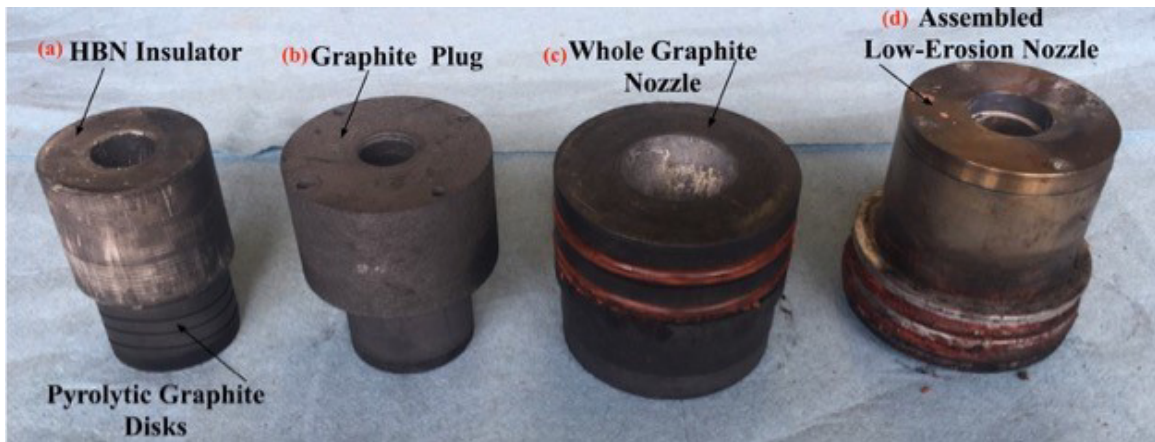


Fig. 3.1: Comparing Alternative Nozzle Configurations

3.2 Thrust Chamber Assembly

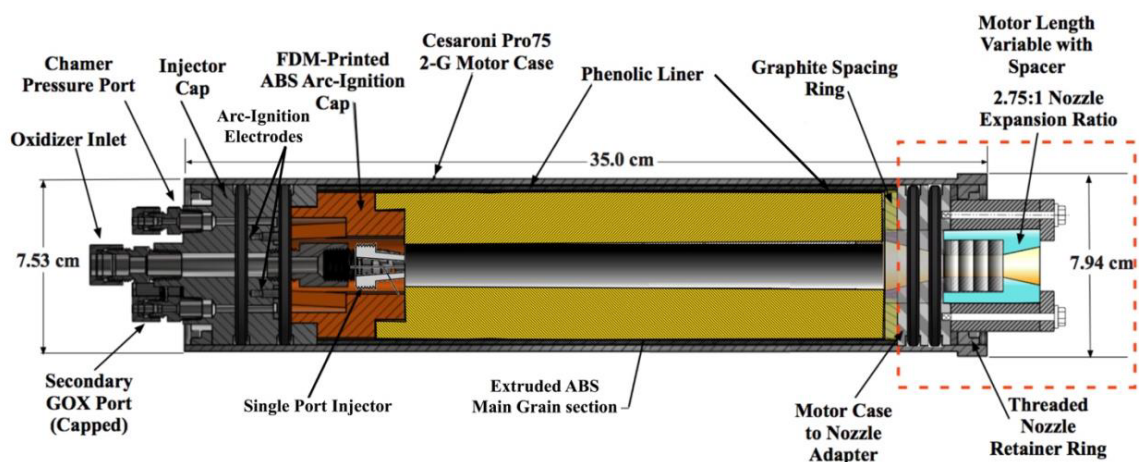


Fig. 3.2: Cutaway View of Thrust Chamber Assembly Showing Low-Erosion Nozzle Interface Details



Fig. 3.3: Thrust Chamber Components

Figure 3.2 shows the composite nozzle configuration mounted to the 75 mm hybrid thrust chamber, adapted from the previously described legacy testing campaign. Figure 3.3 shows the components before assembly. The head end of the fuel grain used a 3-D printed ABS insert for compatibility with the low-energy arc ignition system of the motor [13]. Figure 3.2 shows the thrust chamber assembly as adapted for this test series. Major system components are as follows: 1) nozzle assembly; 2) nozzle retention ring; 3) motor case; 4) 3-D printed ABS ignitor cap with embedded electrodes; 5) extruded ABS main fuel grain section; 6) insulating phenolic liner; 7) chamber pressure fitting; and 8) motor cap with a single-port injector. The 75 mm diameter motor case, constructed from 6061-T6 aluminum, is a commercial off-the-shelf (COTS) Cesaroni Pro75 two-grain motor case.

3.3 Motor Ignition System

The motor ignition system utilizes the Utah-State-University-developed low-wattage arc ignition system. It utilizes the unique electrical properties of fused deposition modeling (FDM) [48] 3-D printed ABS. These properties can be used to allow for rapid on-demand ignition [49].

To use this ignition system and to reduce costs, only the igniter is printed ABS whereas the rest of the fuel grain is machined from high-density extruded ABS. Figure 3.4 shows the detailed schematic of the fuel grain. Figure 3.5 shows the electronic schematic for the

ignition system. An UltraVolt high-voltage power supply is used to produce the voltages necessary to cause the 3-D printed ABS to pyrolyze. Typically, the voltage varies between 100 and 400 volts.

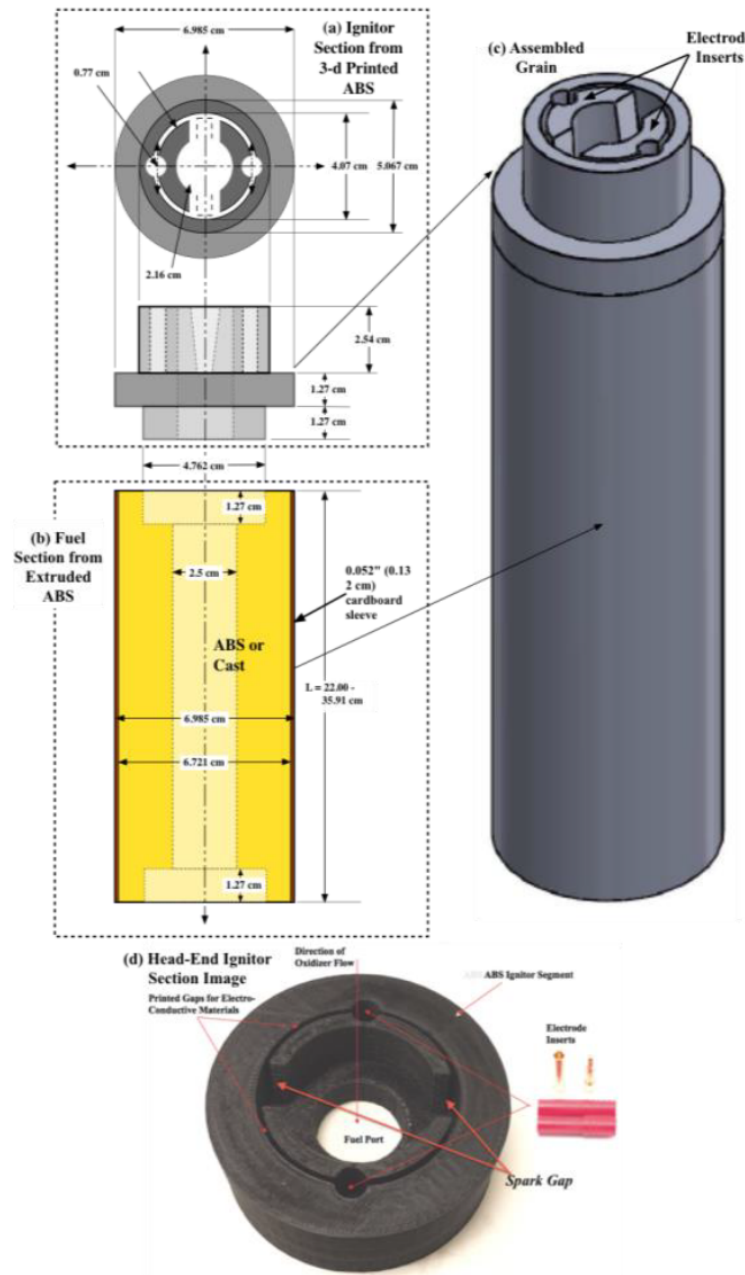


Fig. 3.4: Test Motor Fuel Grain Configuration

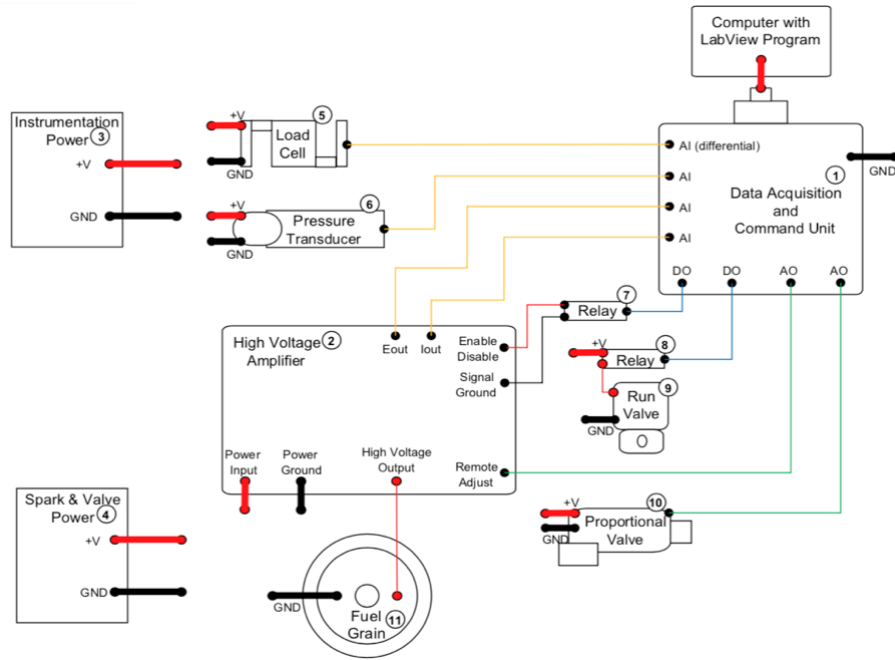


Fig. 3.5: Motor Ignition System for Testing Electronics Layout

3.4 Instrumentation and Test Assembly

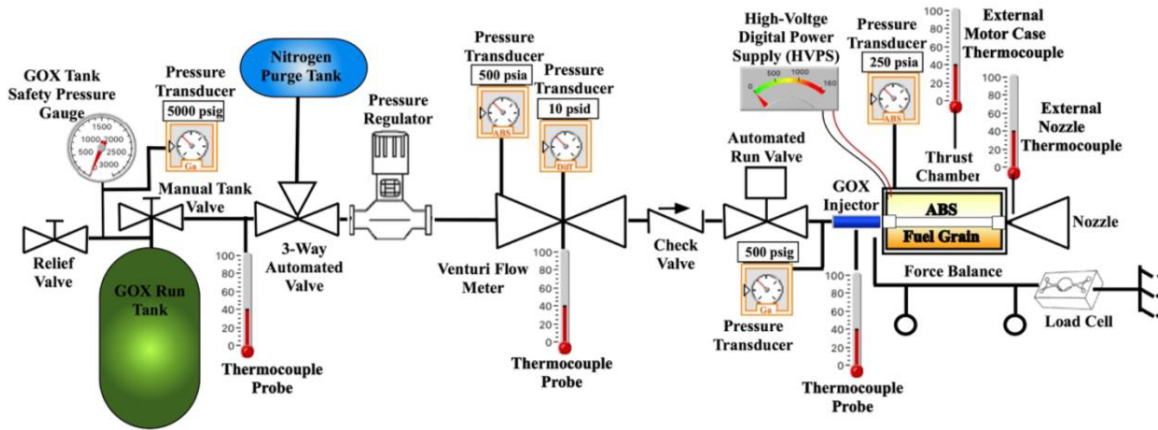


Fig. 3.6: Test Systems Plumbing and Instrumentation Diagram (PID)

Figure 3.6 shows the plumbing and instrumentation diagram (PID) of the experimental apparatus used for this test series. Figure 3.7 shows the test stand. The test stand measurements include: 1) Venturi-based oxidizer mass flow; 2) load-cell-based thrust mea-

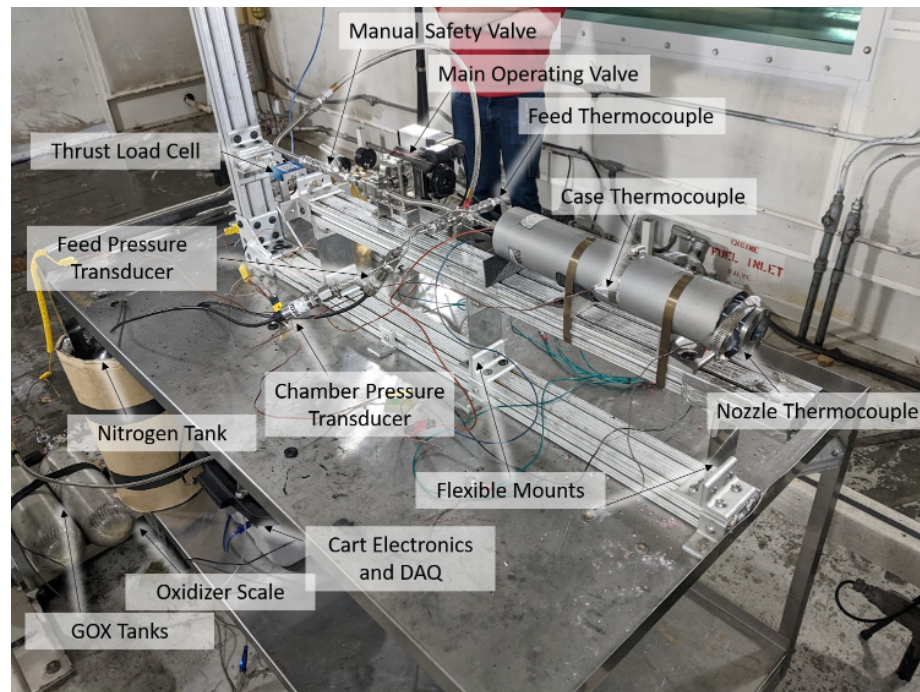


Fig. 3.7: Annotated Test Stand

surements; 3) chamber pressure; 4) GOX tank pressure; 5) injector feed pressure; and 6) multiple temperature readings at various points along the flow path. The motor was mounted to a custom-built and calibrated thrust stand with flexible mounts that allowed thrust transmission in the axial direction. Thrust forces are sensed with a piezoresistive load cell. Custom fire control, data acquisition, and processing software were programmed in National Instruments Labview to ensure run-to-run test consistency, shown in Fig. 3.8.

3.5 Blast Lab Test Stand

All tests were performed in the Battery and Survivability Limits Testing (BLAST) Lab on the Utah State University (USU) campus. The BLAST Lab is a decommissioned Air Force jet test stand that allows for safe observation of rocket test fires from a control room. The rocket test stand in the BLAST Lab is shown in Fig. 3.9. Electronic feedthrough allowed for direct command, control, and data acquisition of all tests.

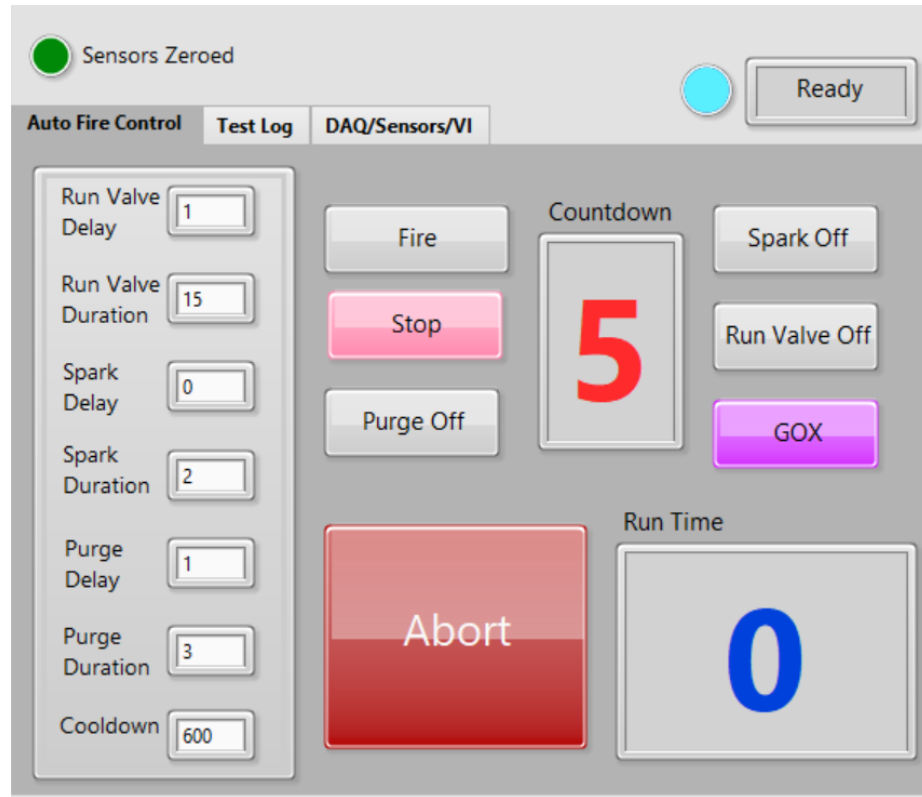


Fig. 3.8: National Instruments Labview Virtual Instrument Front Panel



Fig. 3.9: Test Stand Setup in Blast Lab

CHAPTER 4
ANALYTICAL MODEL

This section contains the analytical methods used to model and support the experimental testing of this thesis. Methods used to model the combustion chemistry and calculate the thermodynamic properties of the combustion plume are presented. Additionally, methods to calculate the key motor parameters derived from raw test data are presented. Finally, a method to calculate nozzle erosion rates is presented.

4.1 Modeling of Combustion Chemistry [1, 2]

NASA's Chemical Equilibrium with Applications (CEA) code [50] was used to model the combustion plume properties. The generic chemical structure of ABS is shown in Fig. 4.1 where N_a , N_b , and N_s are acrylonitrile, butadiene, and styrene respectively. For the high-density extruded ABS fuel, a mole fraction ratio is assumed to be 28.4%, 30.5%, and 41.1% for acrylonitrile, butadiene, and styrene monomers respectively. The monomer ratio was determined using Fourier Transform Infrared (FTIR) analysis performed on a typical high-density extruded ABS sample [51].

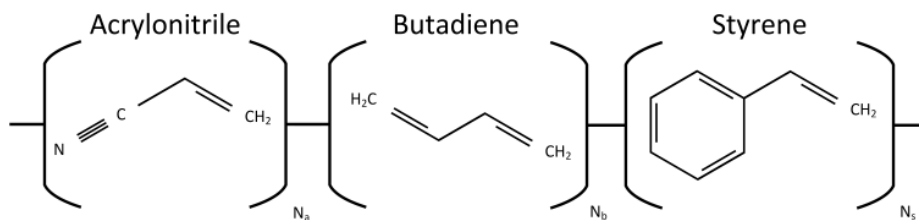


Fig. 4.1: Generic ABS Chemical Structure

$$(C_8H_8)_{0.284} \cdot (C_4H_6)_{0.305} \cdot (C_3H_3N)_{0.411} \quad (4.1)$$

The molecular formula is shown in Eq. (4.1). The corresponding molecular weight M_w is 67.97 g/mol . The enthalpy of formation for ABS fuel was calculated using the group addition method [52]. Using this method the Gibbs free energy is estimated as the summed contributions of the individual molecular group enthalpies of formation minus the associated enthalpies of polymerization. The enthalpy contribution of each monomer $\Delta H_{fmonomer}$, enthalpies of polymerization due to each monomer ΔQ_p , the enthalpy contribution to each polymer of each monomer $\Delta H_{fpolymer}$, the mole fraction of each monomer, and the total enthalpy of formation ΔH_{0f} (63.70 kJ/mol) is shown in Table 4.1. The total enthalpy of formation in terms of kg is 910.4 kJ/kg .

Table 4.1: Enthalpy of Formation for ABS

Monomer	ΔH_f Monomer kJ/mol	ΔQ_f Polymerization kJ/mol	ΔH_f Polymer kJ/mol	Mole Fraction	Enthalpy Contribution kJ/mol
Acrylonitrile	172.62 [53]	74.31 [54]	98.31	0.284	42.27
Butadiene	104.10 [55]	71.10 [56]	32.00	0.305	16.00
Styrene	146.91 [57]	84.60 [54]	63.31	0.411	4.36
ABS Total					63.70

Using ΔH_{0f} from Table 4.1 and molecular formula Eq. (4.1) as inputs, the CEA code calculated the thermodynamics properties for ABS/GOX combustion as a function of combustion pressure and O/F ratio. The CEA-calculated output parameter includes 1) ratio of specific heats (γ); 2) plume exhaust gas constant of proportionality (R_g); 3) combustor stagnation/flame temperature (T_0); 4) molecular weight (M_w); 5) characteristic velocity (c^*); 6) dynamic viscosity (μ); and 7) Prandtl number (P_r).

Figure 4.2 plots the results for T_0 (Fig. 4.2a), M_w (Fig. 4.2b), γ (Fig. 4.2c), and c^* (Fig. 4.2d) as a function of O/F ratio. Individual curves represent varying combustion pressures from 276 kPa to 5515 kPa . The upper and lower combustion pressures are labeled on the graphs.

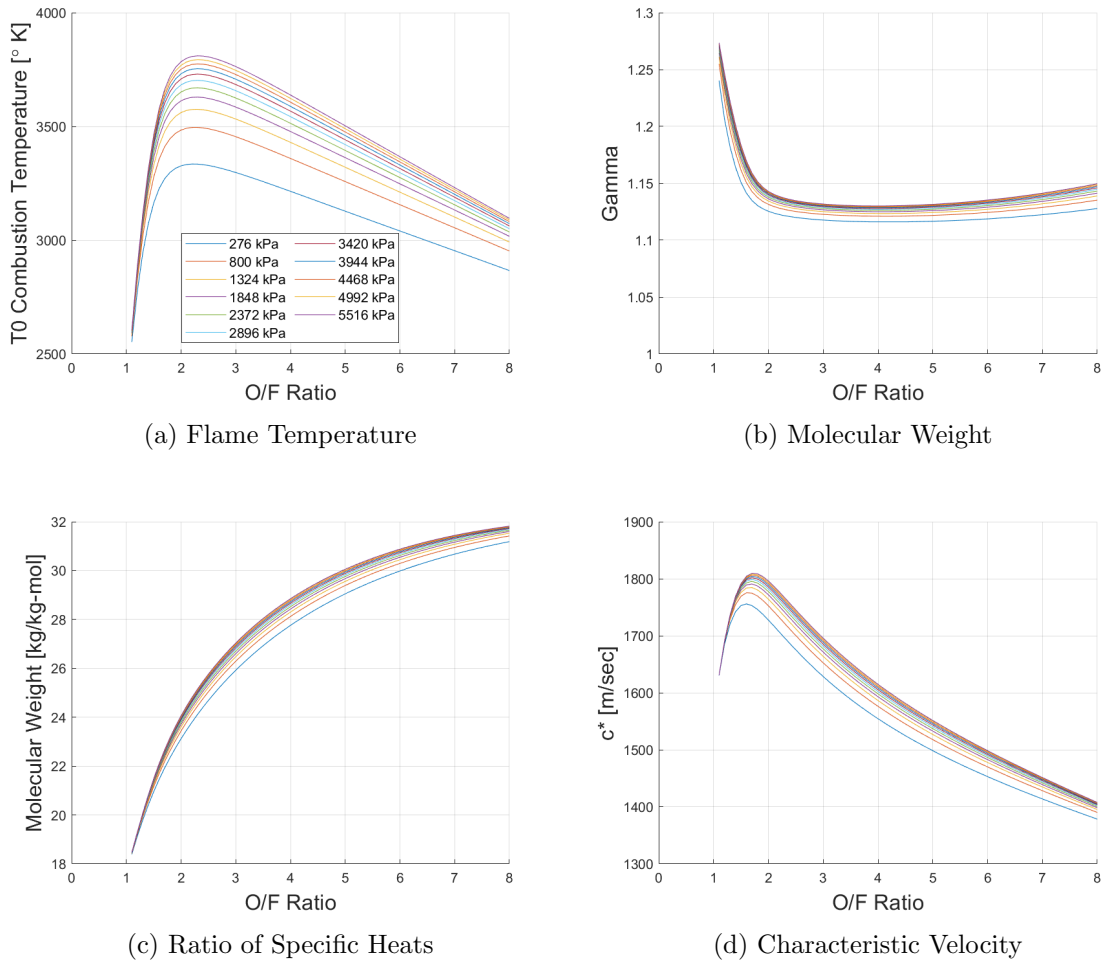


Fig. 4.2: Thermodynamic Properties of GOX/ABS Combustion Products Derived by CEA

4.2 Massflow, O/F, and Equivalence Ratio Calculations [1, 2]

The test apparatus contains an inline Venturi shown in Fig. 3.6. This Venturi measures the oxidizer \dot{m} . There is no real-time measurement of fuel \dot{m} ; instead a total consumed mass was calculated from before and after fuel grain weight measurements. The total mass flow rate, shown in Eq. (4.2), was calculated assuming a constant nozzle throat area A^* (erosion to be included later in this thesis) and the combustion products properties from CEA at each time point using the measured chamber pressure P_0 in the 1-D choking mass flow equation [58].

$$\dot{m}_{total} = A^* P_0 \sqrt{\frac{\gamma}{R_g T_0} \frac{2}{\gamma + 1} \frac{\gamma + 1}{\gamma - 1}} \quad (4.2)$$

For each data point in the burn time history, the 2-D tables of thermodynamic properties of GOX/ABS combustion were interpolated using chamber pressure P_0 and mean O/F as lookup variables. The total consumed fuel mass anchors the thermodynamic calculations. Combustion efficiency is defined in Eq. (4.3).

$$\eta^* = \frac{c_{actual}^*}{c_{ideal}^*} = \frac{\sqrt{\frac{\gamma + 1}{2\gamma} \frac{\gamma + 1}{\gamma - 1} R_g T_{0_{actual}}}}{\sqrt{\frac{\gamma + 1}{2\gamma} \frac{\gamma + 1}{\gamma - 1} R_g T_{0_{ideal}}}} \approx \sqrt{\frac{T_{0_{actual}}}{T_{0_{ideal}}}} \quad (4.3)$$

$$T_{0_{actual}} = T_{0_{ideal}} (\eta^*)^2 \quad (4.4)$$

$$\Delta M_{fuel} = \int_0^T (\dot{m}_{total} - \dot{m}_{ox}) dt \quad (4.5)$$

Where the theoretical flame temperature $T_{0_{ideal}}$ was scaled by adjusting the combustion efficiency, using Eq. (4.4), such that the calculated fuel mass consumption, Eq. (4.5), matches the measured pre- and posttest measurements. The values from Eqs. (4.3) - (4.5) were iterated, adjusting η^* each iteration, until the calculated fuel mass matched the measured fuel mass within 0.5%.

For each iteration, the time average O/F ratio was calculated as integrated oxidizer mass flow divided by consumed fuel mass, Eq. (4.6).

$$\bar{O}/\bar{F} = \frac{\int_0^{t_{burn}} \dot{m}_{ox}(t) dt}{\Delta M_{fuel}} = \frac{\int_0^{t_{burn}} \dot{m}_{ox}(t) dt}{\int_0^{t_{burn}} [\dot{m}_{total}(t) - \dot{m}_{ox}(t)] dt} \quad (4.6)$$

The stoichiometric O/F ratio for a GOX/ABS propellant combination calculated by CEA is approximately 2.917. To calculate the equivalence ratio the stoichiometric O/F ratio is divided by the mean O/F ratio of the burn, shown in Eq. (4.7).

$$\Phi = \frac{(O/F)_{stoich}}{(\bar{O}/\bar{F})} \quad (4.7)$$

As discussed earlier the remaining oxygen in the combustion plume correlates directly with nozzle erosion. Residual oxygen pressure in the plume at the combustor exit is estimated by the mean chamber pressure during the burn divided by the equivalence ratio, Eq. (4.8).

$$P_{pox} = \frac{1}{t_{burn}} \frac{\int_0^{t_{burn}} P_0(t) dt}{\Phi} = \frac{1}{t_{burn}} \frac{(\bar{O}\bar{F}) \int_0^{t_{burn}} P_0(t) dt}{(O/F)_{stoich}} \quad (4.8)$$

4.3 Calculating Nozzle Erosion Rate [1, 2]

Nozzle erosion does not start at the beginning of the burn. Erosion only starts after the surface of the throat reaches a critical temperature for the onset of pyrolysis to begin. The two major factors driving erosion onset timing are combustion O/F ratio and oxidizer partial pressure P_{pox} at the throat, modeled by Eq. (4.8). The nozzle erosion model presented assumes a linear throat area erosion rate ε_{a^*} after the onset of erosion, where $A^*(t)$ is the instantaneous nozzle throat area at time t , A_0^* is the starting throat area, and t_{pyrol} is the pyrolysis onset time, shown in Eq. (4.9).

$$A^*(t) = \begin{cases} A_0^* & t < t_{pyrol} \\ A_0^* + \varepsilon_{A^*}(t - t_{pyrol}) & t \geq t_{pyrol} \end{cases} \quad (4.9)$$

Thrust can be calculated using the 1-D de Laval flow equation [58] based on chamber pressure P_0 in Eq. (4.10). Where p_{exit} is the nozzle exit pressure, p_∞ is the ambient pressure, and A_{exit} is the nozzle exit area.

$$F_{P_0}(t) = P_0(t) A^*(t) \left(\sqrt{\frac{2}{\gamma-1} \frac{2}{\gamma+1} \frac{\gamma+1}{\gamma-1}} \left(1 - \frac{p_{exit}}{P_0} \right)^{\frac{\gamma-1}{\gamma}} + \frac{A_{exit}}{A^*(t)} (p_{exit} - p_\infty) \right) \quad (4.10)$$

With the nozzle throat area remaining constant at A_0^* until pyrolysis onset time the total burn impulse calculated using chamber pressure is presented in Eq. (4.11).

$$\begin{aligned}
I_{P_0} &= \int_0^{t_{burn}} F_{P_0}(t)dt = \int_0^{t_{pyrol}} F_{P_0}(t)dt + \int_{t_{pyrol}}^{t_{burn}} F_{P_0}(t)dt = \\
&\int_0^{t_{pyrol}} \left(\gamma P_0 A_0^* \sqrt{\frac{2}{\gamma-1} \frac{2}{\gamma+1} \frac{\gamma+1}{\gamma-1}} \left(1 - \frac{p_{exit}}{P_0} \right)^{\frac{\gamma-1}{\gamma}} + A_{exit}(p_{exit} - p_\infty) \right) dt + \\
&\int_{t_{pyrol}}^{t_{burn}} \left(\gamma P_0 (A_0^* + \varepsilon_{A^*}(t - t_{pyrol})) \sqrt{\frac{2}{\gamma-1} \frac{2}{\gamma+1} \frac{\gamma+1}{\gamma-1}} \left(1 - \frac{p_{exit}}{P_0} \right)^{\frac{\gamma-1}{\gamma}} + A_{exit}(p_{exit} - p_\infty) \right) dt
\end{aligned} \tag{4.11}$$

The total impulse calculated for load cell thrust measurements is done using Eq. (4.12).

$$I_F = \int_0^{t_{burn}} F(t)dt = \int_0^{t_{pyrol}} F(t)dt + \int_{t_{pyrol}}^{t_{burn}} F(t)dt \tag{4.12}$$

The approximate difference between the two impulse calculations is in Eq. (4.13). This equation assumes that before erosion onset (t_{pyro}) the impulse calculated based on chamber pressure is approximately identical to the load-cell-based impulse.

$$\begin{aligned}
\Delta I_{P\varepsilon_{A^*}} &= I_F - I_{P_0} = \int_0^{t_{pyrol}} F(t)dt + \int_{t_{pyrol}}^{t_{burn}} F(t)dt - \int_0^{t_{pyrol}} F_{P_0}(t)dt - \int_{t_{pyrol}}^{t_{burn}} F_{P_0}(t)dt = \\
&\int_{t_{pyro}}^{t_{burn}} \left(F(t) - \left(\gamma P_0 (A_0^* + \varepsilon_{A^*}(t - t_{pyro})) \sqrt{\frac{2}{\gamma-1} \frac{2}{\gamma+1} \frac{\gamma+1}{\gamma-1}} \left(1 - \frac{p_{exit}}{P_0} \right)^{\frac{\gamma-1}{\gamma}} + A_{exit}(p_{exit} - p_\infty) \right) \right) dt
\end{aligned} \tag{4.13}$$

Assuming an approximately optimal expansion ratio the contribution due to pressure thrust on total impulse calculated with Eq. (4.14) is only weakly dependent on throat erosion and can be ignored.

$$\frac{\partial}{\partial \varepsilon_{A^*}} \left[A_{exit}(p_{exit} - P_\infty) \right] \ll 1 \tag{4.14}$$

Thus, the sensitivity of total impulse to the erosion rate is Eq. (4.15).

$$\frac{\partial I_{P\varepsilon_{A^*}}}{\partial \varepsilon_{A^*}} = \int_{t_{pyrol}}^{t_{burn}} \left(\gamma P_0 (t - t_{pyrol}) \sqrt{\frac{2}{\gamma - 1} \frac{2}{\gamma + 1} \frac{\gamma + 1}{\gamma - 1} \left(1 - \frac{P_{exit}}{P_0} \frac{\gamma - 1}{\gamma} \right)} \right) \quad (4.15)$$

The partial derivative of ε_{A^*} across two successive estimates ($j + 1$) and (j) produce Eq. (4.16).

$$\partial \varepsilon_{A^*} = (\varepsilon_{A^*})^{(j+1)} - (\varepsilon_{A^*})^j \quad (4.16)$$

Approximating the partial derivative of total impulse by the difference between load-cell-based impulse equation Eq. (4.12) and chamber-pressure-based impulse Eq. (4.11) produces Eq. (4.17).

$$\begin{aligned} \partial I_{P\varepsilon_{A^*}} &= I_F - I_P^j = \\ & \int_{t_{pyrol}}^{t_{burn}} \left\{ F(t) - \left(\gamma P_0 (A_0^* + \varepsilon_{A^*} (t - t_{pyrol})) \sqrt{\frac{2}{\gamma - 1} \frac{2}{\gamma + 1} \frac{\gamma + 1}{\gamma - 1} \left(1 - \frac{p_{exit}}{P_0} \frac{\gamma - 1}{\gamma} \right)} + A_{exit} (p_{exit} - p_\infty) \right) \right\} dt \end{aligned} \quad (4.17)$$

Substituting Eqs. (4.16) and (4.17) into Eq. (4.15) and simplifying the step iteration for ε_{A^*} produces Eq. (4.18).

$$\begin{aligned}
(\varepsilon_{A^*})^{(j+1)} &= (\varepsilon_{A^*})^j + \frac{I_F - I_P^j}{\frac{\partial I_P \varepsilon_{A^*}}{\partial \varepsilon_{A^*}} \Big|_j} = \\
& \quad (\varepsilon_{A^*})^j + \\
& \quad \frac{\int_{t_{pyrol}}^{t_{burn}} \left\{ F(t) - \left(\gamma P_0 (A_0^* + \varepsilon_{A^*} (t - t_{pyrol})) \sqrt{\frac{2}{\gamma-1} \frac{2}{\gamma+1} \frac{\gamma+1}{\gamma-1}} \left(1 - \frac{p_{exit}}{P_0} \frac{\gamma-1}{\gamma} \right) + A_{exit} (p_{exit} - p_\infty) \right) \right\} dt}{\int_{t_{pyrol}}^{t_{burn}} \left(\gamma P_0 (t - t_{pyrol}) \sqrt{\frac{2}{\gamma-1} \frac{2}{\gamma+1} \frac{\gamma+1}{\gamma-1}} \left(1 - \frac{P_{exit}}{P_0} \frac{\gamma-1}{\gamma} \right) \right)} dt
\end{aligned} \tag{4.18}$$

Equation (4.18) is equivalent to Newton's method used to find zeros of nonlinear equations. Numerical convergence can be enhanced by including a relaxation parameter $\delta_{A^*} > 1$, shown in Eq. (4.19).

$$(\varepsilon_{A^*})^{(j+1)} = (\varepsilon_{A^*})^j + \frac{I_F - I_P^j}{\delta_{A^*} \frac{\partial I_P \varepsilon_{A^*}}{\partial \varepsilon_{A^*}} \Big|_j} \tag{4.19}$$

Equation (4.19) is solved repeatedly with varying throat area erosion rates at each time step, where the throat area is calculated using Eq. (4.9). The solution is reached when the pressure-transducer-based impulse calculation converges on the force-based impulse calculation. Once the throat area erosion rate is solved then the linear erosion rate can be calculated by Eq. (4.20).

$$A_{(t)}^* - A_0^* = \varepsilon_{A^*} (t - t_{pyrol}) = \pi (r_{t-t_{pyrol}}^2 - r_0^2) = \pi ((r_0 + \dot{r}(t - t_{pyrol}))^2 - r_0^2) \tag{4.20}$$

Solving for \dot{r} in Eq. (4.20) gives Eq. (4.21).

$$\dot{r}_{t_{burn}} = \frac{\sqrt{r_0^2 + \frac{1}{\pi} (t_{burn} - t_{pyrol}) \varepsilon_{A^*}} - r_0}{t_{burn} - t_{pyrol}} \tag{4.21}$$

Equations (4.18) - (4.21) are used to estimate the instantaneous mean throat erosion rate using the measured thrust from the load cell and chamber pressure from a pressure transducer. Because the rate of throat erosion for these tests is fairly small and the burn duration relatively short, this method is considered a more accurate calculation of erosion rates than erosion measurements based on nozzle mass loss or by pretest and post-test throat bore measurements.

CHAPTER 5

TESTING SUMMARY

5.1 Hot Fire Testing Results

This section presents the results of the low-erosion nozzle testing campaign and discusses the importance and context of the testing results. Each nozzle configuration, including the baseline control nozzles, is presented. Throat erosion results are presented for each test configuration. A summary of the testing accomplished for this thesis is in Table 5.1.

5.1.1 Baseline Nozzle Results

In order to provide context and to baseline the test apparatus, two control nozzle configurations were tested. One nozzle configuration was machined from isomolded graphite and the other from RCC. As expected both baseline nozzles experienced significant erosion rates.

Isomolded Graphite Nozzle

The isomolded graphite nozzle, shown in Fig. 5.1a, experience failure after approximately 12 seconds of burn time for two of the three tests. Figure 5.1b shows the structural failure of the graphite nozzle for the first test. Figure 5.2a shows the second test nozzle after the 12-second burn. The failure was due to overheating of the O-rings caused by heat directly conducting conducted from the nozzle throat into the O-rings; the failed O-rings are shown in Fig. 5.2b. The O-ring failure allowed combustion chamber gasses to pass between the nozzle and the combustion chamber.

Table 5.1: Summary of Long-Duration Hybrid Nozzle Testing Campaign

Nozzle	Materials	Number of Tests	Burn Durations	Test Description
Control 1	Monolithic	3	1 - 12 seconds	- Nozzle Failed at 12 seconds for 2/3 burns
	Isomolded		2 - 12 seconds	- High throat nozzle erosion rates
	Graphite		3 - 12 seconds	- High nozzle exit erosion rates
Control 2	Monolithic	2	1 - 12 seconds	- No test structural failure of RCC nozzle
	RCC		2 - 20 seconds	- Survivable burn time exceeding 20 seconds - High nozzle throat erosion rates - High nozzle exit erosion rates
Generation 1	PG-SN Throat, HBN Heat Sink, and SS-316 Shell	7	1 - 5 seconds	
			2 - 10 seconds	- HBN heat sink experienced structural cracking above 15-second burn times
			3 - 15 seconds	- Survivable burn time of approximately 15 seconds
			4 - 15 seconds	- Moderate throat erosion rates
			5 - 15 seconds	- Low nozzle exit erosion rates
			6 - 20 seconds	
			7 - 30 seconds	
Generation 2	PG-HT Throat, HBN Heat Sink, and no SS-316 Shell	3	1 - 10 seconds	- Thermal stress fracture of HBN Shell for 2/3 tests
			2 - 15 seconds	- Multiple HBN fracture points
			3 - 15 seconds	- Survivable burn time of approximately 10 seconds - Very low throat erosion rate - Low nozzle exit erosion rates
Generation 3	PG-HT Throat, RCC Heat Sink, and no SS-316 Shell	6	1 - 10 seconds	- Complete survivability of all tests
			2 - 15 seconds	- Slightly higher erosion rates as compared to Generation 2 nozzle
			3 - 20 seconds	- Moderate nozzle exit erosion rates
			4 - 22 seconds	- RCC heat sink significantly more robust to thermal stress when compared to HBN
			5 - 30 seconds	
			6 - 45 seconds	

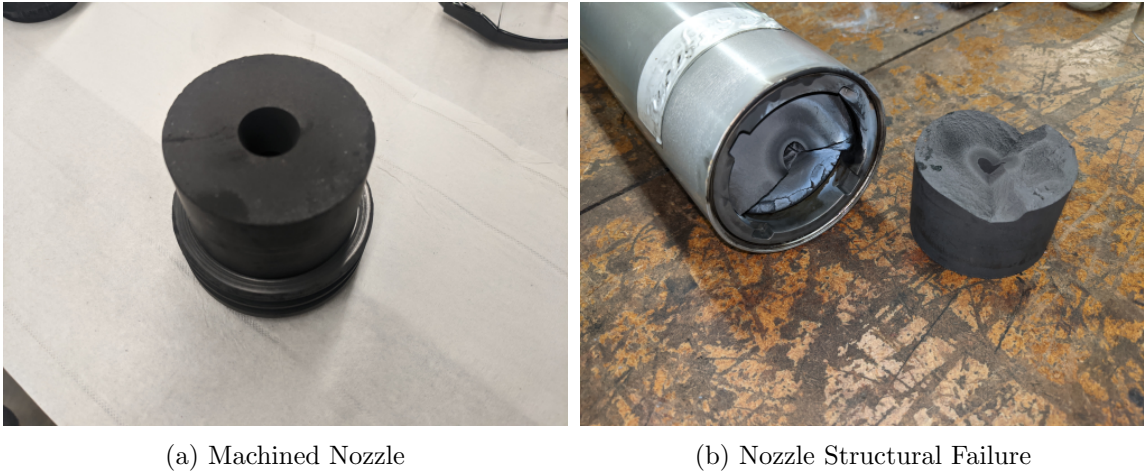


Fig. 5.1: Isomolded Graphite Nozzle 1 Test

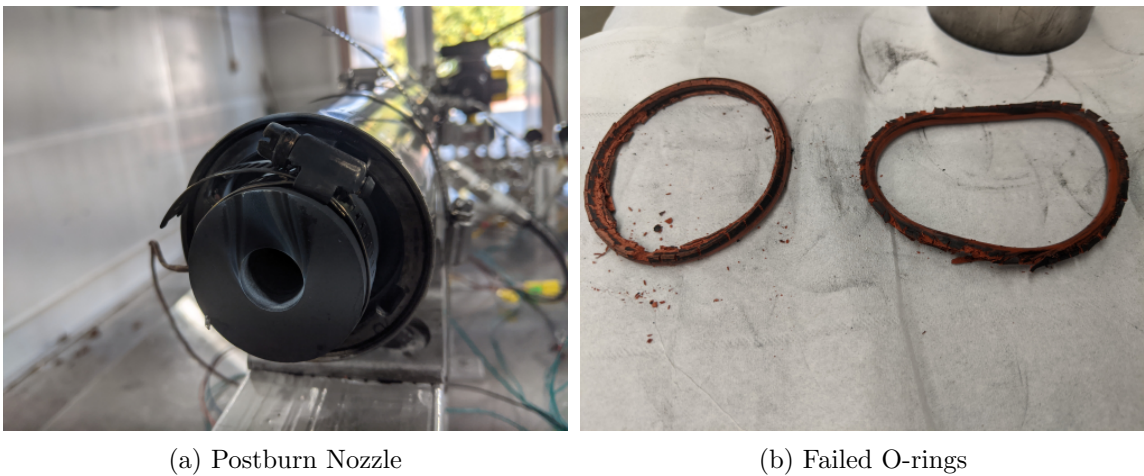


Fig. 5.2: Isomolded Graphite Nozzle 2 Test

RCC Nozzle

The RCC nozzle had no structural failure in either of its two tests and was able to survive a continuous burn time of 20 seconds, though the throat exhibited significant erosion. Figure 5.3 shows the eroded cross-section with a cumulative 32 seconds of burn time. Note the asymmetric erosion of the throat and the erosion of the divergent section of the nozzle, the lower part of the picture, which causes a non-axial thrust component.

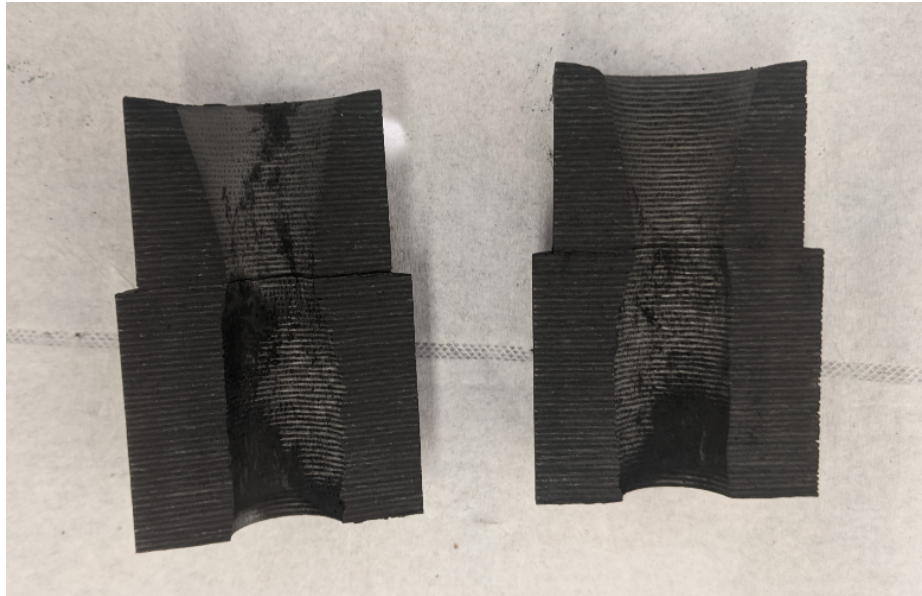


Fig. 5.3: Baseline RCC Nozzle with a Cumulative 32 Seconds of Burn Time

5.1.2 Low-Erosion Nozzles

Generation 1

The first generation nozzle consists of a PG-SN throat and an HBN insulator encased in an SS-316 shell. The full nozzle is shown in Fig. 2.2. This nozzle survived burns up to 15 seconds in duration. The postburn nozzle is shown in Fig. 5.4a. All tests that burned beyond 15 seconds experienced thermally induced structural failure of the HBN section. Figure 5.4b shows the failure pattern of the HBN, failing along radial lines. The PG-SN throat segments did not experience any structural failure and survived with only a small rate of erosion. The postburn PG-SN throat inserts are shown in Fig. 5.5.

Generation 2

The second generation nozzle consisted of a PG-HT throat along with an HBN insulator with no SS-316 shell, shown in Fig. 5.6. The HBN had a structural failure for two of the three 15-second tests. PG-HT had a significant reduction in throat erosion rate over the PG-SN. The added heat transfer to the HBN along with the absence of the SS-316 shell resulted

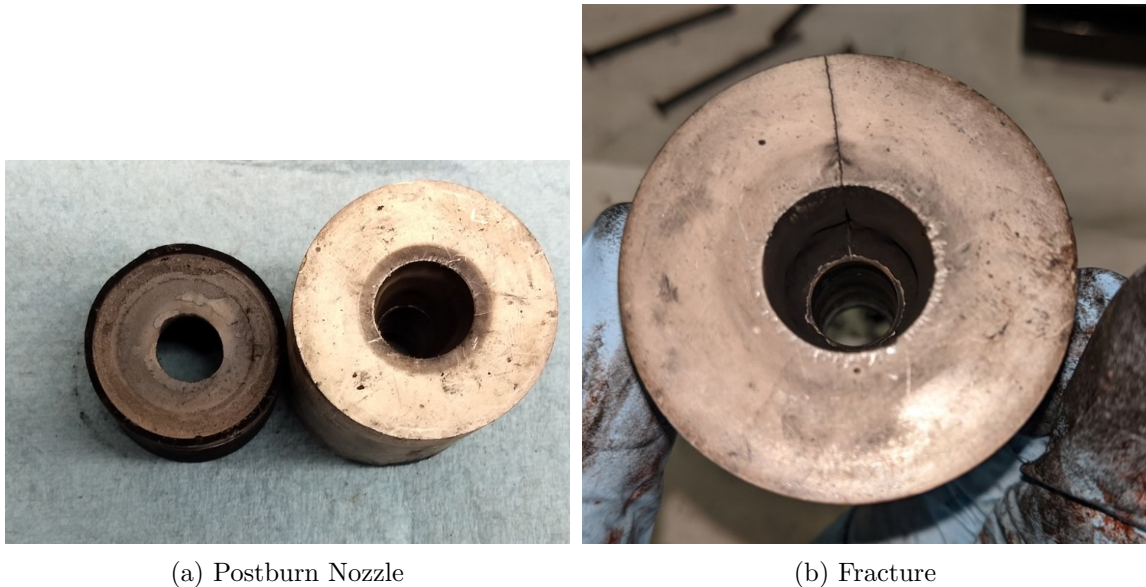


Fig. 5.4: Generation 1 Nozzle



Fig. 5.5: PG-SN Throat Inserts

in multiple fracture points in the HBN. The larger coefficient of thermal expansion (CTE) and elastic modulus of the PG-HT inserts were also likely contributors to the high-stress levels in the HBN layer of the second generation. Fracture patterns of the second generation nozzle are shown in Fig. 5.7. No second generation nozzle survived burn durations beyond 15 seconds.

Generation 3

The third generation consisted of a PG-HT throat with an RCC insulator and no SS-316 shell, shown in Fig. 5.8. This configuration survived burn times of up to 30 seconds.

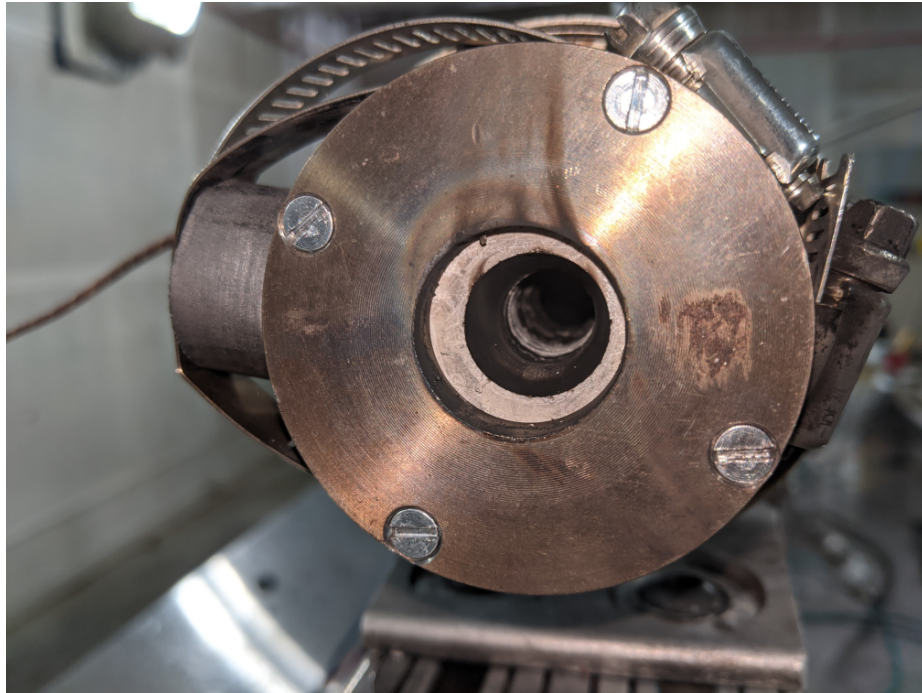


Fig. 5.6: Generation 2 Nozzle



(a) Burn 2 Fracture

(b) Burn 3 Fracture

Fig. 5.7: Generation 2 Nozzle Failure

The erosion rate of the throat was slightly higher as compared to the second generation nozzle but the RCC was significantly more resistant to the thermal stresses as compared to HBN. The RCC in the third configuration of the nozzle appears to be a good compromise of material strength and erosion resistance of the throat.

The PG-HT throat inserts showed significantly reduced erosion rates when compared to the PG-SN inserts. Figure 5.9 compares the PG-SN and PG-HT throat inserts following a series of 20-second burns. The PG-HT cross-section is less eroded and exhibits better circular symmetry when compared to the PG-SN inserts. The higher thermal conductivity inserts reduce overall erosion and delay the onset of pyrolysis resulting in a more uniform cross-section.

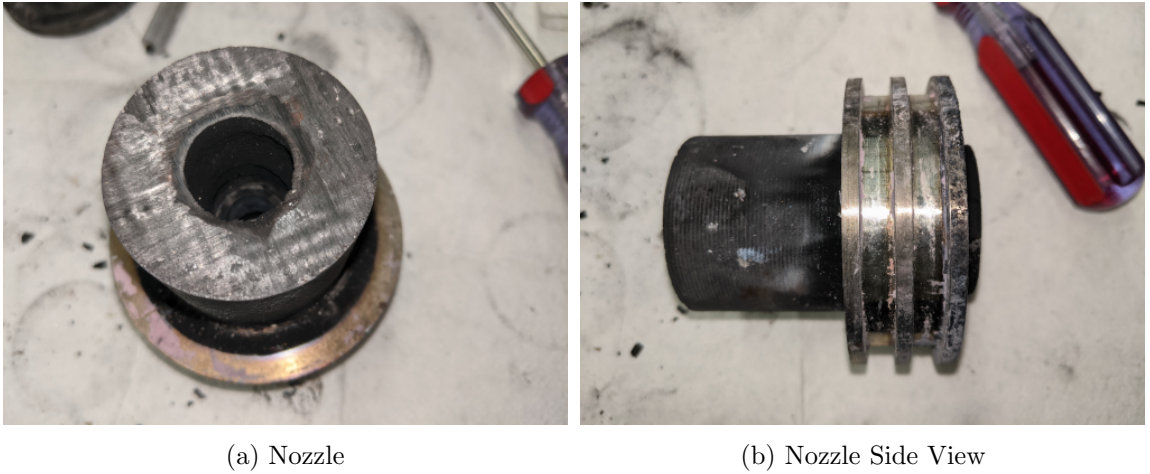


Fig. 5.8: Generation 3 Nozzle

5.2 Erosion Analysis and Discussion [2]

To observe the effects of nozzle erosion on in-flight real-time thrust estimation the load cell thrust measurement time history was compared to the thrust derived from measured chamber pressure time history and the 1-D de Laval flow equations [58], assuming constant nozzle throat area. Equations (4.18), (4.21), and (5.1) were used to correct the measured chamber pressure for nozzle erosion. Where $D^*(t)_\epsilon$ is the eroded throat diameter, D_0^* is the initial throat diameter, and $U(\tau_\epsilon)$ is a unit step function that is zero if $\tau_\epsilon < t_{pyro}$ and a value of 1 if $\tau_\epsilon \geq t_{pyro}$.

$$D^*(t)_\epsilon = D_0^* + 2(t - \tau_\epsilon)\dot{r}_\epsilon U(\tau_\epsilon) \quad (5.1)$$

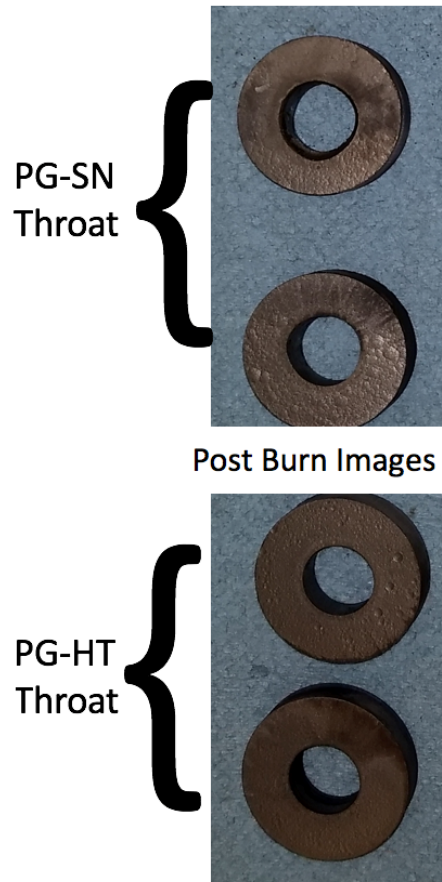


Fig. 5.9: Postburn Comparisons of PG-SN and PG-HT Nozzle Throat Inserts

Figures 5.10 through 5.14 compare the different configurations. Figures 5.10a, 5.11a, 5.12a, 5.13a, and 5.14a show the difference between the load cell measured thrust, the white line, and the calculated thrust using the de Laval equations from the chamber pressure not accounting for nozzle erosion, the red line. Figures 5.10b, 5.11b, 5.12b, 5.13b, and 5.14b compare the load cell measured thrust, the white line, to the thrust calculated using the de Laval equations from the chamber pressure but incorporating the calculate nozzle erosion from Eqs. (4.18), (4.21), and (5.1), the red line.

The monolithic isomolded graphite nozzle and the monolithic RCC nozzle, Figs. 5.10 and 5.11, both show significant nozzle erosion. This erosion can be seen in the deviation between the white and red lines with erosion onset occurring between five and seven seconds after motor start in Figs. 5.10a and 5.11a.

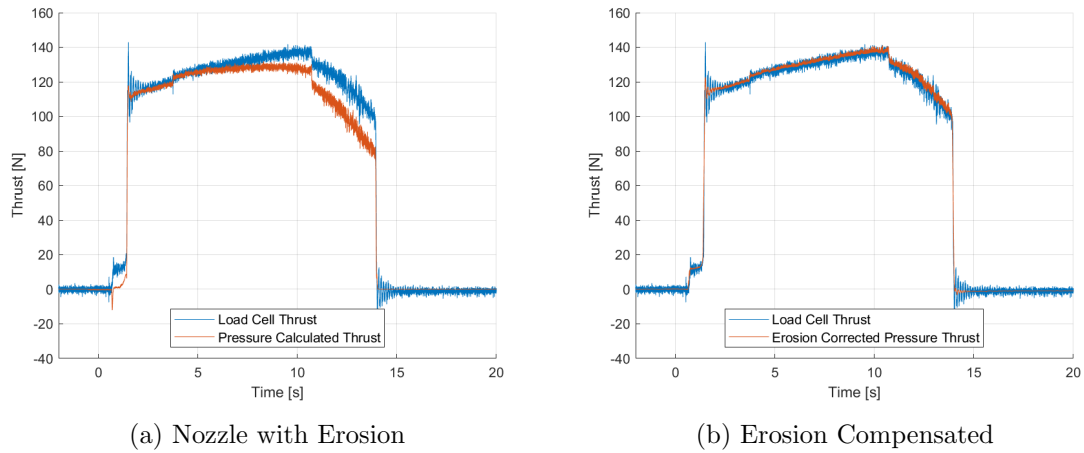


Fig. 5.10: Effects of Nozzle Erosion on Calculated Thrust Profiles for Monolithic Isomolded Graphite Nozzle

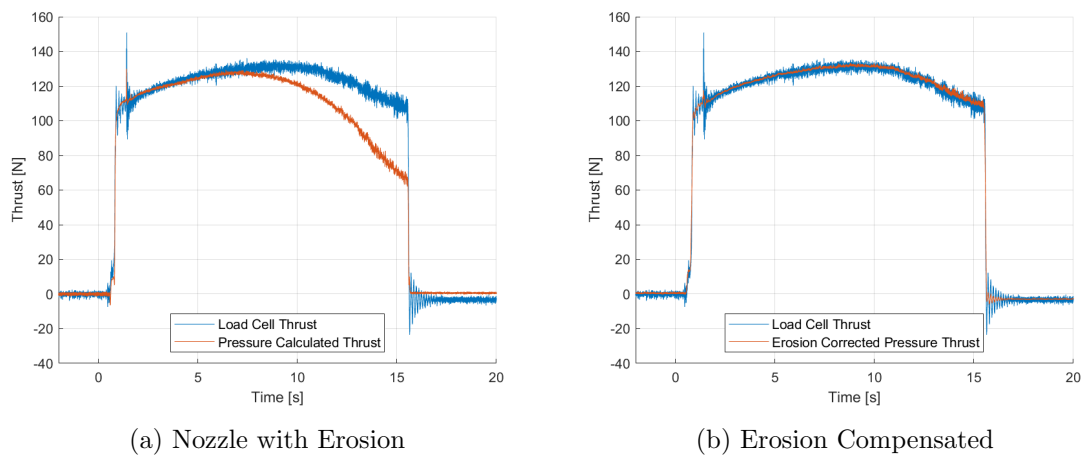


Fig. 5.11: Effects of Nozzle Erosion on Calculated Thrust Profiles for Monolithic RCC Nozzle

The first generation nozzle, PG-SN/HBN/SS-316, shows a reduced erosion rate over the 15-second burn duration when compared to the monolithic nozzles, as can be seen in Fig. 5.12. The second generation nozzle, PG-HT/HBN, showed significantly reduced erosion, over the 15-second burn, where essentially no erosion occurred shown in Fig. 5.13. The third generation nozzle, PG-HT/RCC, showed an increased rate of erosion as compared to the second generation nozzle but had a reduced erosion rate when compared to the first generation nozzle, as seen in Fig. 5.14.

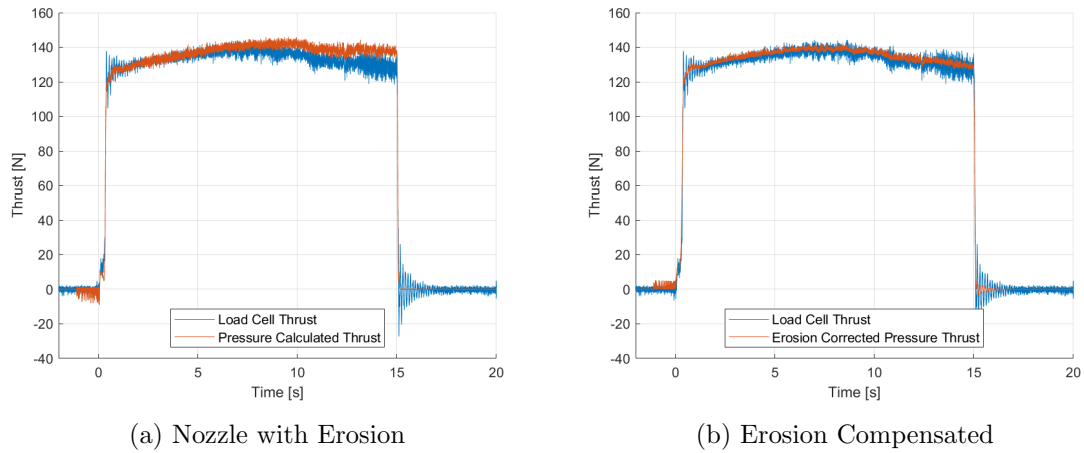


Fig. 5.12: Effects of Nozzle Erosion on Calculated Thrust Profiles for Generation 1 Nozzle Configuration

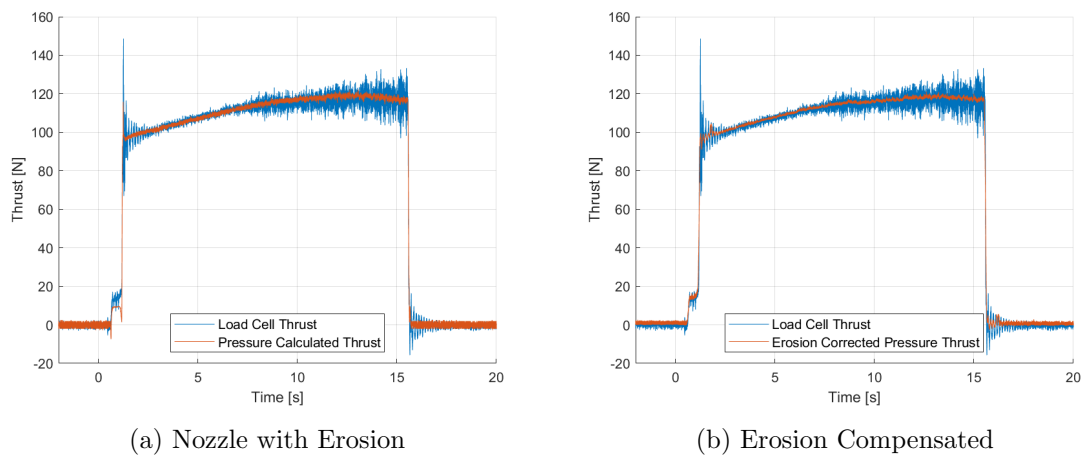


Fig. 5.13: Effects of Nozzle Erosion on Calculated Thrust Profiles for Generation 2 Nozzle Configuration

Figure 5.15 compares the erosion onset time for different equivalence ratios for the five nozzle configurations tested. Figure 5.16 compares the erosion rates for different equivalence ratios for the five nozzle configurations tested. Additionally, points derived from data from a series of tests performed by Karaman [59] are plotted. These tests show data for a GOX and paraffin rocket motor with a graphite nozzle. Figure 5.16 additionally plots analytical erosion rate predictions from Bianchi and Nasuti [24] for a GOX and HTPB propellant and a graphite nozzle.

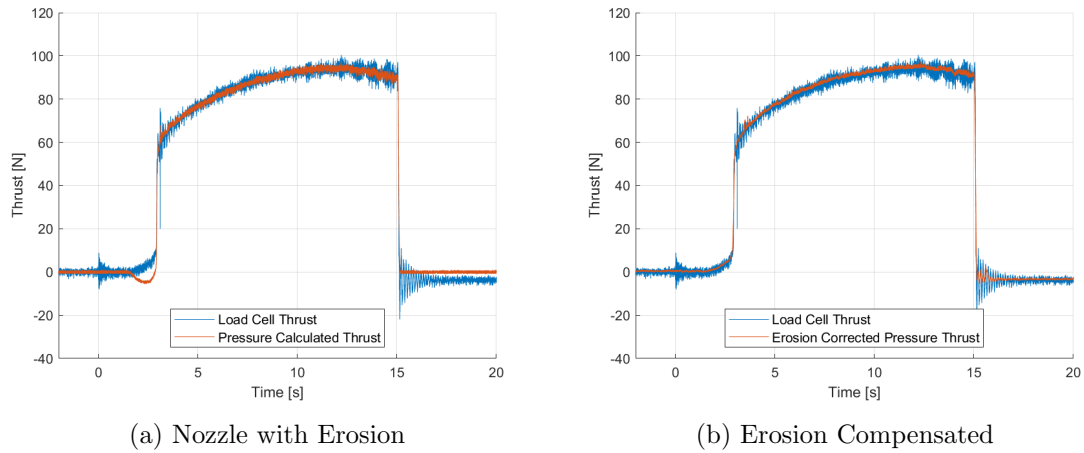


Fig. 5.14: Effects of Nozzle Erosion on Calculated Thrust Profiles for Generation 3 Nozzle Configuration

For lower equivalence ratios, and the corresponding lean burning conditions, the monolithic isomolded graphite and monolithic RCC nozzles experience rapid erosion onset and high erosion rates. At higher equivalence ratios, where there is a richer burn condition, the onset time of erosion increases and the erosion rates drop. All three generations of the low-erosion nozzle experienced a significant reduction in erosion rate along with an increase in erosion onset time. It is observed that the second generation nozzle, PG-HT/HBN, exhibited the lowest overall erosion with the third generation, PG-HT/RCC, slightly higher than it and the first generation, PG-SN/HBN/SS-316, slightly higher than the third generation. Since the RCC of the third generation nozzle is much more robust to thermal stresses, compared to the HBN, the third generation nozzle is a good compromise of low throat erosion and material survivability for long-duration burns.

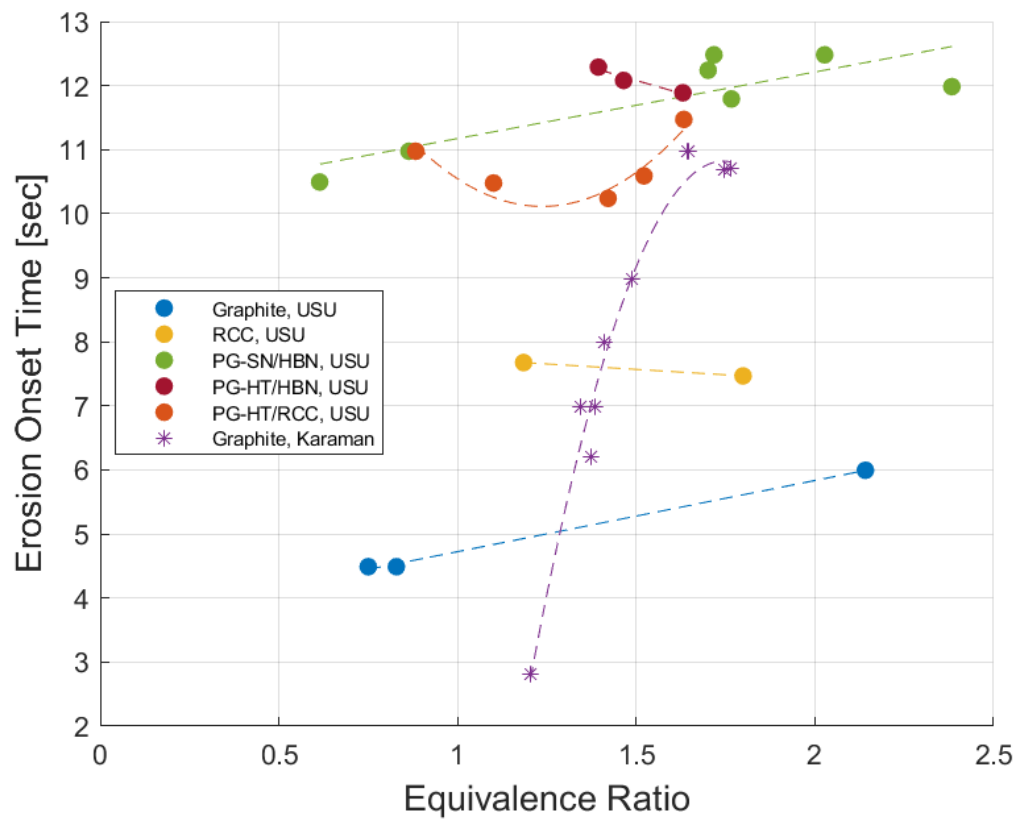


Fig. 5.15: Erosion Onset Time for Various Nozzle Materials

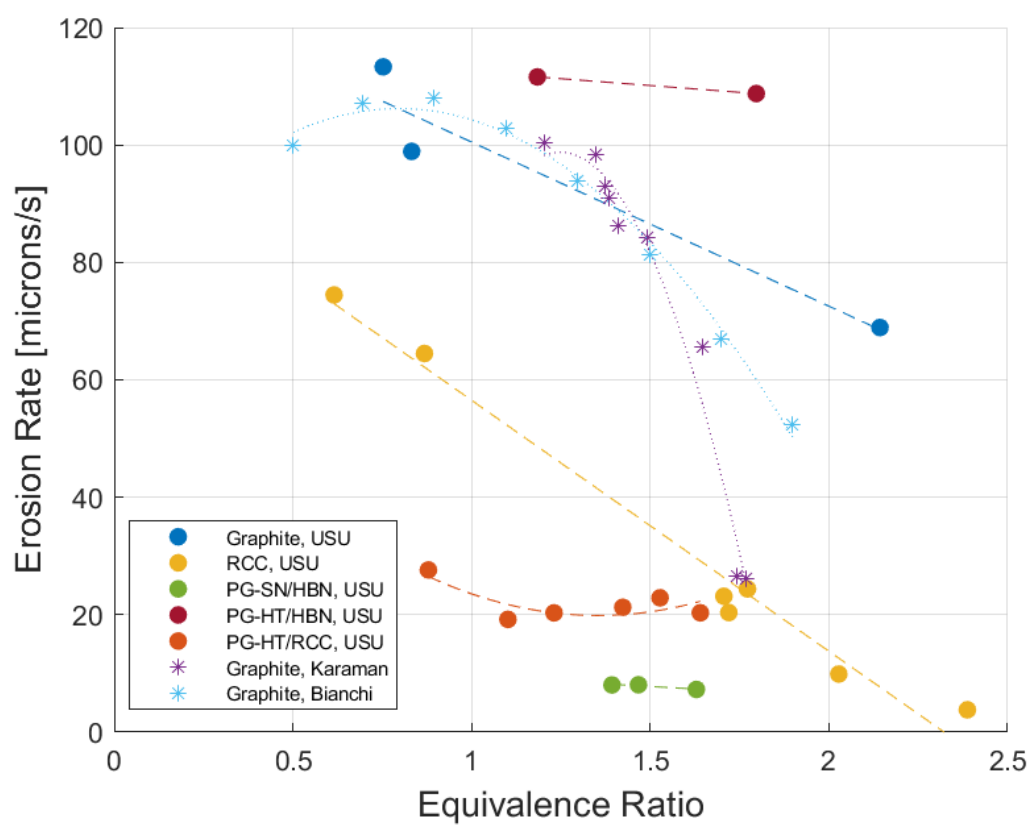


Fig. 5.16: Erosion Rate for Various Nozzle Materials

CHAPTER 6

CONCLUSION

The effects of nozzle erosion have long been ignored for modeling hybrid rocket stage trajectories. Neglecting this has the potential to compromise accurate calculations of hybrid power systems for optimal trajectories. Since continuous nozzle throat enlargement during a burn directly affects the engine thrust profile, consumed propellant mass, and overall vehicle mass, it is essential to include the effects of nozzle throat erosion in overall hybrid propulsion system modeling, design, simulation, and trajectory optimization. Nozzle throat area uncertainty increases as burn length increases. The effects of this uncertainty produce significant variability in motor performance. A low-erosion nozzle system designed for hybrid motor systems is needed.

This thesis presents results from proof of concept tests of low-erosion nozzle configurations specifically designed for hybrid motors. The designs utilized highly anisotropic material properties of pyrolytic graphite, hexagonal boron nitride, and reinforced carbon-carbon to reduce the temperature of nozzle throat material to increase the time for erosion onset and to reduce overall nozzle erosion. Tests were three generations of nozzles. First was a PG-SN nozzle throat with a HBN heat sink layer and a SS-316 supporting shell. The second generation used PG-HT material for the throat along with an HBN heat sink layer. Finally, the third generation used the PG-HT throat and replaced the HBN with RCC for the heat sink.

Test results from multiple long-duration burns were compared against a monolithic isomolded graphite nozzle and a monolithic RCC nozzle. The low-erosion nozzles showed a five-fold decrease in erosion rates. Due to large thermal gradients in the low-erosion nozzles and mismatched thermal expansion, the HBN material would crack due to excessive stresses. The first generation nozzle experienced fewer failure rates when compared to the second due to the SS-316 support shell and the lower thermal expansion rate of PG-SN

compared to PG-HT. The HBN heat sink material did not survive burns longer than 15 seconds in length in the first generation nozzle and could only survive up to 10 seconds of burn time for the second generation nozzle.

To increase survivability RCC was used as a drop-in replacement for the HBN in the second generation nozzle. RCC has significantly higher material strength properties. In addition, the thermal expansion rate was more closely matched to the PG-HT than the HBN. The third generation nozzle using the RCC also utilized PG-HT, which has a higher radial heat transfer coefficient when compared to PG-SN and is thus able to transfer more heat away from the nozzle throat surface delaying pyrolysis.

Test results verify that the third generation nozzle, PG-HT/RCC, design exhibits significant long-duration burn survivability when compared to the first two generations of nozzle designs. The third generation nozzle did not experience structural failure during any of the burns and survived burn times of up to 30 seconds. Due to the lower heat capacity of the RCC heat sink the third generation nozzle did exhibit higher throat erosion than the second generation nozzle. However, when structural serviceability is considered, there is a reasonable trade-off concerning erosion reduction, thermal expansion strains, and material strength for the third generation nozzle.

6.1 Future Work

Due to the COVID-19 pandemic, the USU propulsion lab was unable to perform all planned tests. There lacks both a depth and breath of testing volume and conditions. To continue improving the long-duration low-erosion hybrid nozzle the accompanying analytical models additional testing should be performed. Specifically, preventing fracturing of the HBN insulator while keeping the nozzle light weight and increasing the burn time capability of a low-erosion nozzle.

REFERENCES

- [1] Whitmore, S. A., Babb, R. S., Gardner, T. J., LLOYD, K. P., and Stephens, J. C., “Pyrolytic Graphite and Boron Nitride as Low-Erosion Nozzle Materials for Long-Duration Hybrid Rocket Testing,” *AIAA Propulsion and Energy 2020 Forum*, AIAA Propulsion and Energy Forum, American Institute of Aeronautics and Astronautics, Aug. 2020.
- [2] Whitmore, S. A., Babb, R., Stephens, J. C., and Horlacher, J. D., “Further Development of Low-Erosion Nozzle Materials for Long-Duration Hybrid Rocket Burns,” *AIAA Propulsion and Energy 2021 Forum*, American Institute of Aeronautics and Astronautics, eprint: <https://arc.aiaa.org/doi/pdf/10.2514/6.2021-3514>.
- [3] “Hazard Analysis Of Commercial Space Transportation. Volume 1: Operations; Volume 2: Hazards; Volume 3: Risk Analysis,” Tech. Rep. PB93199040, U.S. Department of Commerce, May 1988.
- [4] Sutton, G. P. and Biblarz, O., *Rocket propulsion elements*, John Wiley & Sons, 7th ed.
- [5] Dornheim, M., “Reaching 100 km,” Vol. 161, Aug. 2004, pp. 45–46.
- [6] Casalino, L. and Pastrone, D., “Optimization of Hybrid Sounding Rockets for Hypersonic Testing,” *Journal of Propulsion and Power*, Vol. 28, No. 2, March 2012, pp. 405–411, Publisher: American Institute of Aeronautics and Astronautics.
- [7] Casalino, L. and Pastrone, D., “Optimal Design of Hybrid Rocket Motors for Microgravity Platform,” *Journal of Propulsion and Power*, Vol. 24, No. 3, May 2008, pp. 491–498, Publisher: American Institute of Aeronautics and Astronautics.
- [8] Jens, E., Karp, A. C., Nakazono, B., Eldred, D. B., DeVost, M. E., and Vaughan, D., “Design of a Hybrid CubeSat Orbit Insertion Motor,” *52nd AIAA/SAE/ASEE Joint Propulsion Conference*, AIAA Propulsion and Energy Forum, American Institute of Aeronautics and Astronautics, July 2016.
- [9] Casalino, L. and Pastrone, D., “A Straightforward Approach for Robust Design of Hybrid Rocket Engine Upper Stage,” *51st AIAA/SAE/ASEE Joint Propulsion Conference*, AIAA Propulsion and Energy Forum, American Institute of Aeronautics and Astronautics, July 2015.
- [10] Karp, A. C., Nakazono, B., Benito Manrique, J., Shotwell, R., Vaughan, D., and Story, G. T., “A Hybrid Mars Ascent Vehicle Concept for Low Temperature Storage and Operation,” *52nd AIAA/SAE/ASEE Joint Propulsion Conference*, AIAA Propulsion and Energy Forum, American Institute of Aeronautics and Astronautics, July 2016.
- [11] Whitmore, S. A., Peterson, Z. W., and Eilers, S. D., “Closed-Loop Precision Throttling of a Hybrid Rocket Motor,” *Journal of Propulsion and Power*, Vol. 30, No. 2, March 2014, pp. 325–336, Publisher: American Institute of Aeronautics and Astronautics.

- [12] Whitmore, S. A., Spurrier, Z. S., Walker, S. D., and Merkley, S. L., “Throttled Launch-Assist Hybrid Rocket Motor for an Airborne NanoSat Launch Platform,” *52nd AIAA/SAE/ASEE Joint Propulsion Conference*, American Institute of Aeronautics and Astronautics, eprint: <https://arc.aiaa.org/doi/pdf/10.2514/6.2016-4658>.
- [13] Whitmore, S. A., Inkley, N. R., Merkley, D. P., and Judson, M. I., “Development of a Power-Efficient, Restart-Capable Arc Ignitor for Hybrid Rockets,” *Journal of Propulsion and Power*, Vol. 31, No. 6, Nov. 2015, pp. 1739–1749, Publisher: American Institute of Aeronautics and Astronautics.
- [14] Whitmore, S. A., Mathias, S., and Harvey, R., “High Voltage Breakdown and Arc-Tracking Mechanism of Thermoplastics with Applications to Hybrid Rocket Arc-Ignition,” *53rd AIAA/SAE/ASEE Joint Propulsion Conference*, AIAA Propulsion and Energy Forum, American Institute of Aeronautics and Astronautics, July 2017.
- [15] Whitmore, S. A., Merkley, S. L., Tonc, L., and Mathias, S. D., “Survey of Selected Additively Manufactured Propellants for Arc Ignition of Hybrid Rockets,” *Journal of Propulsion and Power*, Vol. 32, No. 6, Nov. 2016, pp. 1494–1504, Publisher: American Institute of Aeronautics and Astronautics.
- [16] Whitmore, S. A. and Bulcher, A. M., “A Green Hybrid Thruster Using Moderately Enriched Compressed Air as the Oxidizer,” *2018 Joint Propulsion Conference*, AIAA Propulsion and Energy Forum, American Institute of Aeronautics and Astronautics, July 2018.
- [17] Pastrone, D. and Casalino, L., “Integrated Design-Trajectory Optimization for Hybrid Rocket Motors,” *Modeling and Optimization in Space Engineering*, edited by G. Fasano and J. D. Pintér, Springer Optimization and Its Applications, Springer, New York, NY, 2013, pp. 343–362.
- [18] Pastrone, D. and Casalino, L., “Optimal Robust Design of Hybrid Rocket Engines,” *Space Engineering: Modeling and Optimization with Case Studies*, edited by G. Fasano and J. D. Pintér, Springer Optimization and Its Applications, Springer International Publishing, Cham, 2016, pp. 269–285.
- [19] Casalino, L., Masseni, F., and Pastrone, D., “Uncertainty Analysis and Robust Design for a Hybrid Rocket Upper Stage,” *Journal of Spacecraft and Rockets*, Vol. 56, No. 5, Sept. 2019, pp. 1424–1431, Publisher: American Institute of Aeronautics and Astronautics.
- [20] Betts, J. T., “Survey of Numerical Methods for Trajectory Optimization,” *Journal of Guidance, Control, and Dynamics*, Vol. 21, No. 2, March 1998, pp. 193–207, Publisher: American Institute of Aeronautics and Astronautics.
- [21] DeLuca, L., Galfetti, L., Maggi, F., and Colombo, G., “Advances in Hybrid Rocket Propulsion,” Vol. 6, pp. 1–10.
- [22] Kuo, K. K. and Chiaverini, M. J., editors, *Fundamentals of Hybrid Rocket Combustion and Propulsion*, American Institute of Aeronautics and Astronautics, Reston, VA, May 2007.

- [23] Bunker, R. and Prince, A., “Hybrid rocket motor nozzle material predictions and results,” *28th Joint Propulsion Conference and Exhibit*, Joint Propulsion Conferences, American Institute of Aeronautics and Astronautics, July 1992.
- [24] Bianchi, D. and Nasuti, F., “Numerical Analysis of Nozzle Material Thermochemical Erosion in Hybrid Rocket Engines,” *Journal of Propulsion and Power*, Vol. 29, No. 3, May 2013, pp. 547–558, Publisher: American Institute of Aeronautics and Astronautics.
- [25] Boysan, M. E., “Analysis of regenerative cooling in liquid propellant rocket engines,” Journal Abbreviation: Sıvı yakıtlı roket motorlarında rejeneratif soğutma analizleri.
- [26] Berry, J. M. and Gebhardt, J. J., “Mechanical properties of pyrolytic graphite,” Vol. 3, No. 2, pp. 302–308.
- [27] Lemak, R., Moskaitis, R., Pickrell, D., Kupp, D., and Yocum, A., “High Performance Pyrolytic Graphite Heat Spreaders – Near Isotropic Structures and Metallization,” Vol. 1158, pp. 1158, Publisher: Cambridge University Press.
- [28] Shackelford, J. F., *CRC materials science and engineering handbook*, CRC Press, Taylor & Francis Group, fourth edition ed.
- [29] Sichel, E. K., Miller, R. E., Abrahams, M. S., and Buiocchi, C. J., “Heat capacity and thermal conductivity of hexagonal pyrolytic boron nitride,” Vol. 13, No. 10, pp. 4607–4611.
- [30] Accuratus, “Boron Nitride | BN Material Properties,” retrieved 28 April 2021. <http://accuratus.com/boron.html>.
- [31] Luo, R., Liu, T., Li, J., Zhang, H., Chen, Z., and Tian, G., “Thermophysical properties of carbon/carbon composites and physical mechanism of thermal expansion and thermal conductivity,” Vol. 42, No. 14, pp. 2887–2895.
- [32] Peters, S. T., *Handbook of Composites*, Springer Science & Business Media.
- [33] Store, G., “PG-SN Grade Pyrolytic Graphite,” retrieved 28 April 2021. <http://www.graphitestore.com/core/media/media.nl?id=9192&c=4343521&h=5e5c593978206523306a>.
- [34] Martens, H. E. and Jaffe, L. D., “Tensile Strength of Pyrolytic Graphite up to 2750°C,” Vol. 31, No. 6, pp. 1122–1122.
- [35] Levy, M., “Oxidation of Pyrolytic Graphite in Air between 1250° and 1850° F.” Vol. 1, No. 1, pp. 19–23.
- [36] Ohmori, J., Kobayashi, T., Yamada, M., Iida, H., and Horie, T., “Mechanical behavior of graphite first wall during disruptions,” Vol. 9, pp. 201–205.
- [37] Shinno, H., Kitajima, M., and Okada, M., “Thermal stress analysis of high heat flux materials,” Vol. 155-157, pp. 290–294.

- [38] Berry, J. M. and Gebhardt, J. J., “Mechanical properties of pyrolytic graphite,” Vol. 3, No. 2, pp. 302–308.
- [39] Elements, A., “Pyrolytic Graphite,” retrieved 28 April 2021. <https://www.americanelements.com/pyrolytic-graphite-7782-42-5>.
- [40] Store, G., “PG-HT Grade Pyrolytic Graphite,” retrieved 28 April 2021. <http://www.graphitestore.com/core/media/media.nl?id=9420&c=4343521&h=be85398b10991db920f5>.
- [41] Kim, C. S., “Thermophysical properties of stainless steels,” <http://www.osti.gov/servlets/purl/4152287/>.
- [42] “Grade 316 Stainless Steel Technical Data,” retrieved 28 April 2021. <https://askzn.co.za/stainless-steel/tech-grade-316.htm>.
- [43] “Properties: Stainless Steel - Grade 316 (UNS S31600),” retrieved 28 April 2021. <https://www.azom.com/properties.aspx?ArticleID=863>.
- [44] Whitmore, S. A., Armstrong, I. W., Heiner, M. C., and Martinez, C. J., “High-Performing Hydrogen Peroxide Hybrid Rocket with 3-D Printed and Extruded ABS Fuel,” *2018 Joint Propulsion Conference*, AIAA Propulsion and Energy Forum, American Institute of Aeronautics and Astronautics, July 2018.
- [45] Whitmore, S. A., Martinez, C. J., and Markley, D. P., “Catalyst development for an arc-ignited hydrogen peroxide/ABS hybrid rocket system,” *Aeronautics and Aerospace Open Access Journal*, Vol. Volume 2, No. Issue 6, Nov. 2018, Publisher: MedCrave Publishing.
- [46] Pappis, J. and Blum, S. L., “Properties of Pyrolytic Graphite,” *Journal of the American Ceramic Society*, Vol. 44, No. 12, 1961, pp. 592–597, eprint: <https://ceramics.onlinelibrary.wiley.com/doi/pdf/10.1111/j.1151-2916.1961.tb11664.x>.
- [47] Bhimanapati, G. R., Glavin, N. R., and Robinson, J. A., “Chapter Three - 2D Boron Nitride: Synthesis and Applications,” *Semiconductors and Semimetals*, edited by F. Iacopi, J. J. Boeckl, and C. Jagadish, Vol. 95 of *2D Materials*, Elsevier, Jan. 2016, pp. 101–147.
- [48] Peterson, E., “Fused Deposition Modeling: Most Common 3D Printing Method,” .
- [49] Whitmore, S. A., Inkley, N. R., Merkley, D. P., and Judson, M. I., “Development of a Power-Efficient, Restart-Capable Arc Ignitor for Hybrid Rockets,” *Journal of Propulsion and Power*, Vol. 31, No. 6, Nov. 2015, pp. 1739–1749, Publisher: American Institute of Aeronautics and Astronautics.
- [50] Gordon, S. and McBride, B. J., “Computer program for calculation of complex chemical equilibrium compositions and applications. Part 1: Analysis,” Oct. 1994, NTRS Author Affiliations: NASA Lewis Research Center NTRS Report/Patent Number: NAS 1.61:1311 NTRS Document ID: 19950013764 NTRS Research Center: Legacy CDMS (CDMS).

- [51] Whitmore, S. A. and Mathias, S. D., “Optimizing 3-D Printable Hybrid Fuels by Blending of Immiscible Polymers,” *2018 Joint Propulsion Conference*, AIAA Propulsion and Energy Forum, American Institute of Aeronautics and Astronautics, July 2018.
- [52] van Krevelen, D. W. and Chermin, H. A. G., “Estimation of the free enthalpy (Gibbs free energy) of formation of organic compounds from group contributions,” *Chemical Engineering Science*, Vol. 1, No. 2, Dec. 1951, pp. 66–80.
- [53] Baxendale, J. H. and Madaras, G. W., “Kinetics and heats of copolymerization of acrylonitrile and methyl methacrylate,” *Journal of Polymer Science*, Vol. 19, No. 91, 1956, pp. 171–179, eprint: <https://onlinelibrary.wiley.com/doi/pdf/10.1002/pol.1956.120199117>.
- [54] Carraher, C. E. and Seymour, R. B., *Seymour/Carraher’s polymer chemistry*, No. 16 in Undergraduate chemistry, M. Dekker, New York, 6th ed., 2003.
- [55] van Krevelen, D. W. and Nijenhuis, K. t., *Properties of Polymers: Their Correlation with Chemical Structure; their Numerical Estimation and Prediction from Additive Group Contributions*, Elsevier.
- [56] Prosen, E., Maron, F., and Rossini, F., “Heats of combustion, formation, and isomerization of ten C4 hydrocarbons,” *Journal of Research of the National Bureau of Standards*, Vol. 46, No. 2, Feb. 1951, pp. 106.
- [57] Prosen, E. J. and Rossini, F. D., “Heats of formation and combustion of 1, 3-butadiene and styrene,” *Journal of Research of the National Bureau of Standards*, Vol. 34, No. 1, 1945, pp. 59–63, Publisher: US GOVERNMENT PRINTING OFFICE SUPERINTENDENT DOCUMENTS, WASHINGTON, DC.
- [58] Anderson, J. D., *Modern compressible flow: with historical perspective*, Vol. 3, McGraw-Hill New York, 2003.
- [59] Kahraman, B., Karakas, H., Eren, B. N., and Karabeyoglu, A., “Erosion Rate Investigation of Various Nozzle Materials in Hybrid Rocket Motors,” *AIAA Propulsion and Energy 2020 Forum*, 2020, p. 3739.